Universidad Autónoma de Nuevo León
Facultad de Ciencias Químicas

Morphology effect of noble metal nanostructures on the performance of on-line surface-enhanced Raman spectroscopy microfluidic chips

Por

M.C. CARLOS EDUARDO PUENTE DE LEÓN

Como requisito parcial para obtener el Grado de
DOCTOR EN CIENCIAS con orientación en
Química de los materiales

Junio, 2022

RESUMEN

Carlos Eduardo Puente de León Fecha de graduación: Junio, 2022

Universidad Autónoma de Nuevo León

Facultad de Ciencias Químicas

Título del estudio: Morphology effect of noble metal nanostructures on the performance of on-line surface-enhanced Raman spectroscopy microfluidic chips

Número de páginas: 90 Candidato para el Grado de Doctor en Ciencias con Orientación en Química de los Materiales

Área de estudio: Nanoquímica

Propósito y Método del Estudio: En la constante búsqueda por métodos analíticos de mayor sensibilidad y menor costo, la espectroscopía Raman aumentada en superficies resalta por detectar analitos a concentraciones tan bajas que incluso se ha alcanzado la detección de una sola molécula; si además, se aprovechan las cualidades de un estudio microfluídico como el uso de bajo volumen, condiciones de flujo constante, y la posibilidad de tratamiento de la muestra dentro del chip, entonces obtendremos una técnica con la sensibilidad de SERS y la reproducibilidad y miniaturización de la microfluídica. En este trabajo se fabricaron chips microfluídicos decorados con nanoestructuras de Ag con diferentes morfologías y se estudió su actividad SERS.

Contribuciones y Conclusiones: Chips microfluídicos decorados con nanopartículas de Ag para ser usados como sustratos SERS de alta sensibilidad, fabricados en PDMS-vidrio y acrílico. Los sustratos SERS alcanzaron límites de detección menores a 10^{-8} M para *p*-aminotiofenol como analito.

Firma del asesor:____

ACKNOWLEDGMENTS

Al Dr. Israel Alejandro López Hernández por su constante apoyo y confianza, y por empujarme a aprender cosas nuevas que nunca creí podría aprender.

Al Dr. Gabriel Caballero Robledo y al Cinvestav por su apoyo durante la estancia de investigación, y por abrir las puertas de su laboratorio aun cuando la pandemia avanzaba.

A CONACyT por la beca otorgada.

A mi familia, por su apoyo incondicional y motivación.

A mis amigos, quienes me han ayudado en esos momentos de tristeza, me han levantado cuando todo parecía ir mal, me hicieron reír, y me impulsaron a querer ser una mejor persona. A todos ellos, gracias, los llevo siempre conmigo.

TABLE OF CONTENTS

Chapter **Page**

TABLE LIST

Table **Page**

FIGURE LIST

Figure **Page**

NOMENCLATURE

LSP	Localized surface plasmon
LSPR	Localized surface plasmon resonance
SERS	Surface-enhanced Raman spectroscopy
IR	Infrared
$\boldsymbol{P}$	Electric dipole moment
a	Polarizability
R	Detector position
θ	Detector diameter
n	Refraction index
d	Particle diameter
λ	Laser wavelength
MF-SERS	Microfluidic SERS
PDMS	Polydimethylsiloxane
SLA	Stereolithography
ABS	Acrylonitrile butadiene styrene
PLA	Polylactic acid
PET	Polyethylene terephthalate
STL	Standard triangle language

EF	Enhancement factor
LOD	Detection limit
UV-Vis	Ultraviolet-visible
FE-SEM	Field-emission scanning electron microscopy
TEM	Transmission electron microscopy
CNC	Computerized Numerical Control
M	mol/L
rpm	Revolutions per minute
DMAB	4,4’-dimercaptoazobenzene

CHAPTER 1

INTRODUCTION

1.1 Plasmonic materials

Among the novel materials, the metallic nanostructures attracted special attention due to their unique properties that differ greatly from their bulk counterparts. These properties are caused by the quantum confinement of the material in one or more dimensions, causing a different behavior of their electrons and interactions. When an electromagnetic wave interacts with a nanoscaled-metallic particle, the electron cloud of the material oscillates coherently with this wave; a quantum of this oscillation is known as plasmon, and its formation, changes, and applications are studied by the plasmonics science. Particularly, when the particle is too small in such a way that the plasmon can not be propagated through the material, nor to an external material or medium, the plasmon is called localized surface plasmon (LSP), and its resonance (LSPR) is the base of the most interesting properties of this kind of materials. Fig. 1 shows a representation of a plasmon produced in a small metallic nanosphere.

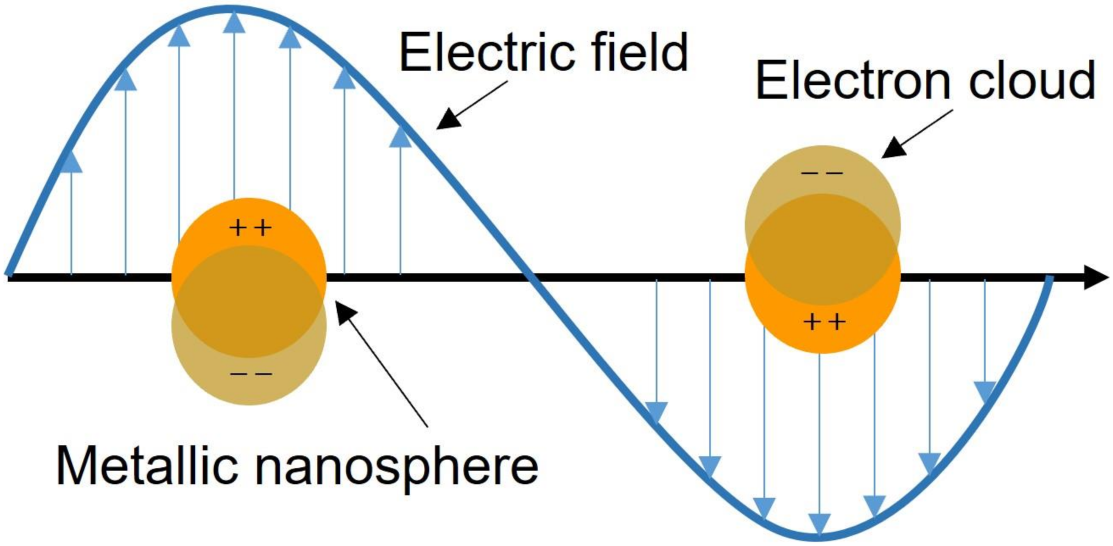

Fig. 1 Representation of a plasmon in a metallic nanosphere.

Although the mainly used plasmonic materials are Ag and Au nanostructures, the formation of plasmons can be observed in the coinage elements, as well as in some aluminum and carbon-based materials. However, the wavelengths required for the plasmon resonances differ from one material to another, ranging from the ultraviolet to far-infrared wavelengths. As the LSPR wavelengths required for the excitation of Ag and Au nanoparticle plasmons are mainly in the visible to the near-infrared range, these metals became rapidly the symbol of the plasmonic materials. This wavelength range, at the same time, represents the area of interest of many spectrophotometric techniques that uses light to analyze compounds or samples for their determination, characterization, or quantification.

Nevertheless, it is widely known that the optical properties of plasmonic materials depend on different factors such as their morphology (size, shape, and polydispersity) and chemical environment, as shown in Fig. 2; therefore, their properties can be tuned by changing any of these parameters [1-3]. Talking about tuning the morphology of a dispersion, this can be done by using different reagents and physical parameters; for example, using reductors with different reducing power can lead to a change in the nuclei formation rate and thus, the availability of the remaining metallic ions will be crucial to allow nuclei growth and determine if the final dispersion is composed of a high concentration of small seeds or a system with a smaller number of bigger particles. On the other hand, the interactions between the metallic nuclei and the stabilizing molecules allow their bonding in specific crystalline planes, acting as barriers that lead to growth in specific planes and directions, producing nanostructures with defined shapes and sizes such as nanorods, nanoplates, and even geometrical shapes as cubes and octahedra.

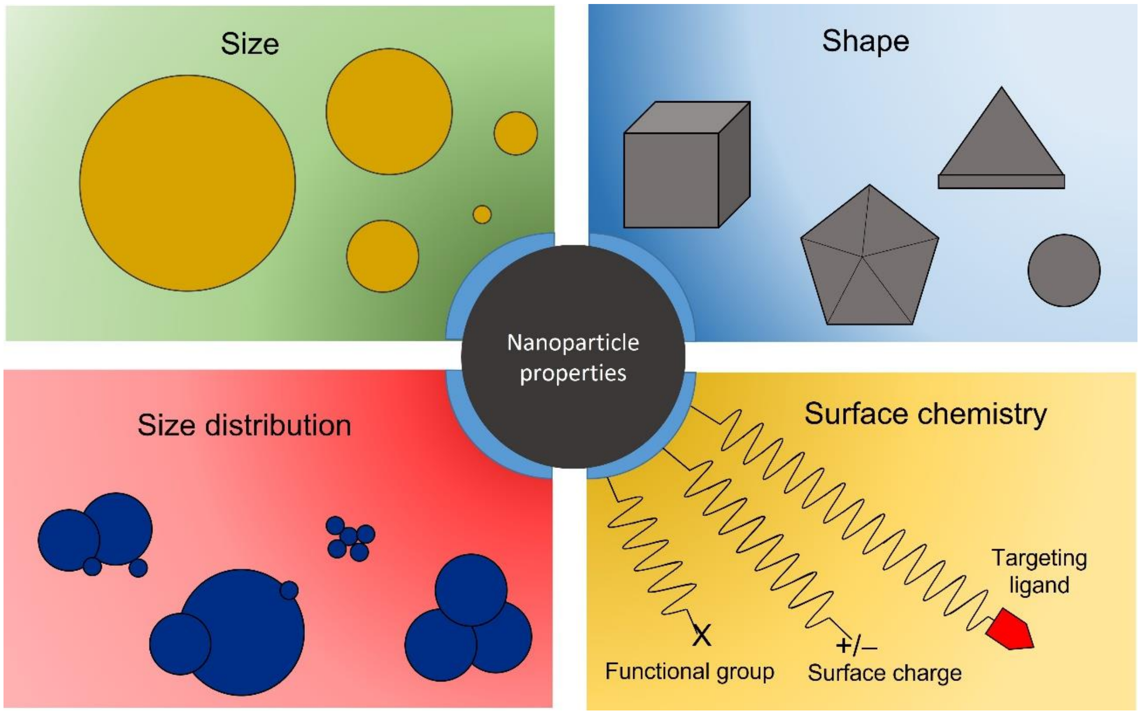

Fig. 2 Representation of the main factors that affect the properties of a nanoparticle dispersion.

The latter opens a wide opportunity for the development of new materials based on nanostructures with different morphologies and specific properties for any application or use [4-7]; an example is the fabrication of devices, substrates, or products that can enhance the selectivity, sensitivity, or multidetection capability of analytical techniques [8-10]. This can be observed in the use of noble metal nanostructures with tunable properties in substrates for surface-enhanced Raman spectroscopy (SERS) to increase the intensity of the Raman bands produced by the analyte molecules [11]. This enhancement is produced when the nanoparticles themselves act as nanoantennas due to the excitation of their plasmon modes and amplifies the signals produced by molecular vibrations [12-14].

1.2 Raman and surface-enhanced Raman spectroscopies

The Raman spectroscopy is a vibrational technique that retrieves information about the stretching and bending modes of the analyte functional groups, this is possible by detecting the inelastic scattering (or Raman scattering) of incident light. In this technique, a laser interacts with the sample, exciting it to a virtual energy state and thus producing vibrational activity of the moieties; however, as some of the photon energy was used for the vibrations, it now contains a different frequency and energy. If this photon energy is lower, and the molecule now is at a higher state than its initial state, a Stokes scattering occurred; if the outcome is a photon with higher energy and a molecule at a lower state, then an anti-Stokes scattering occurred, this can be better understood by analyzing the Jablonski diagram shown in Fig. 3.

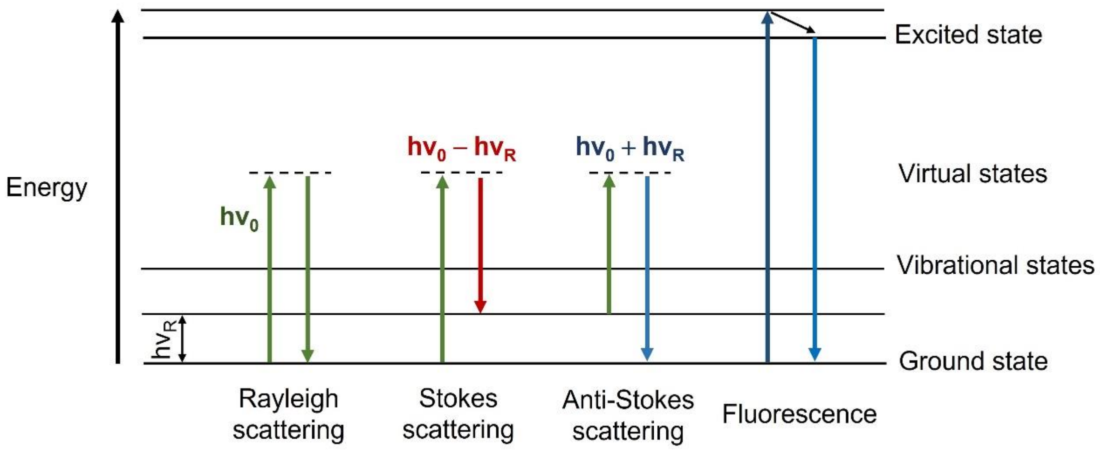

Fig. 3 Jablonski diagram of the electronic transitions that might occur during a Raman analysis.

The vibrational modes of matter are known to be studied by infrared spectroscopies (IR), yet, performing Raman studies lead to complementary information about the sample due to their fundaments difference. IR can detect vibrations produced by a change in the electric dipolar moment (***P***) of the molecule, whereas Raman spectroscopy detects any change in the sample polarizability (α), which means that the electron cloud shape must change to be detected. Therefore, it is common to find vibrational modes that are not observed in IR but can be observed in Raman, and vice versa.

The intensity of light scattered by a particle can be calculated using the detector position (R), diameter (θ), refraction index (n), particle diameter (d), and laser wavelength (λ) as indicated in the following equation:

$$I = I_0 \frac{1+\cos^2\theta}{2R^2} \left(\frac{2\pi}{\lambda}\right)^4 \left(\frac{n^2-1}{n^2+2}\right) \left(\frac{d}{2}\right)^6 \qquad (1)$$

However, the detector parameters are usually fixed and cannot be changed in a Raman study performance, therefore, the Raman intensity is inversely proportional to the laser wavelength:

$$I \propto \frac{1}{\lambda^4} = \lambda^{-4} \tag{2}$$

There are different lasers that can be used for this spectroscopy, and its importance not only lies on the intensity of the vibrational bands, as the laser energy can affect the resonance of different vibrations and energetic processes such as fluorescence. The most used lasers are the 532, 633, 785, and 1064 nm, but some others can be used depending on the energy required to analyze a specific sample, even UV lasers can be useful. Also, as fluorescence may occur when an excess of energy is applied to the sample, changing the laser can reduce or eliminate this interference. Yet, it is important to understand that the spectra obtained with different lasers may be shifted or changed in any way.

As each molecule is chemically different, the Raman spectrum is a fingerprint of the analyzed species, being capable to distinguish even between allotropic and polymorphic structures. This makes the Raman spectroscopy a powerful technique for the determination and characterization of a wide range of samples, among which we can mention proteins, herbicides, dyes, explosives, biological compounds, among other chemical species of interest for diseases, security, sensing, reaction tracking and other applications [15-18]. Despite this, the probability of a photon to be inelastically scattered is low, leading to low Raman intensities, and thus, making the spectrum hard to analyze. A way to approach this problem is the use of SERS substrates, which as mentioned before, lead to higher intensities.

SERS is a technique based on the use of plasmonic nanoparticles to enhance the Raman signal produced, reaching intensities enhancements as high as 10^6 times the value that can be obtained using neat Raman spectroscopy; also, research works regarding the detection of a single molecule can be found in the literature. These increases in Raman performance are caused by two mechanisms: the charge transfer mechanism and the electromagnetic mechanism [19], which are illustrated in Fig. 4. In the first case, “hot” electrons are transferred between the excited plasmons and the analyte orbitals, increasing the probability to produce Raman scattered photons; however, the molecules must have direct contact with the nanostructures on the substrate. Also, the enhancements produced greatly varies depending on the system conditions: this mechanism becomes more important when an external source of energy is applied to the system; nevertheless, in a regular Raman analysis, this mechanism leads to low enhancements.

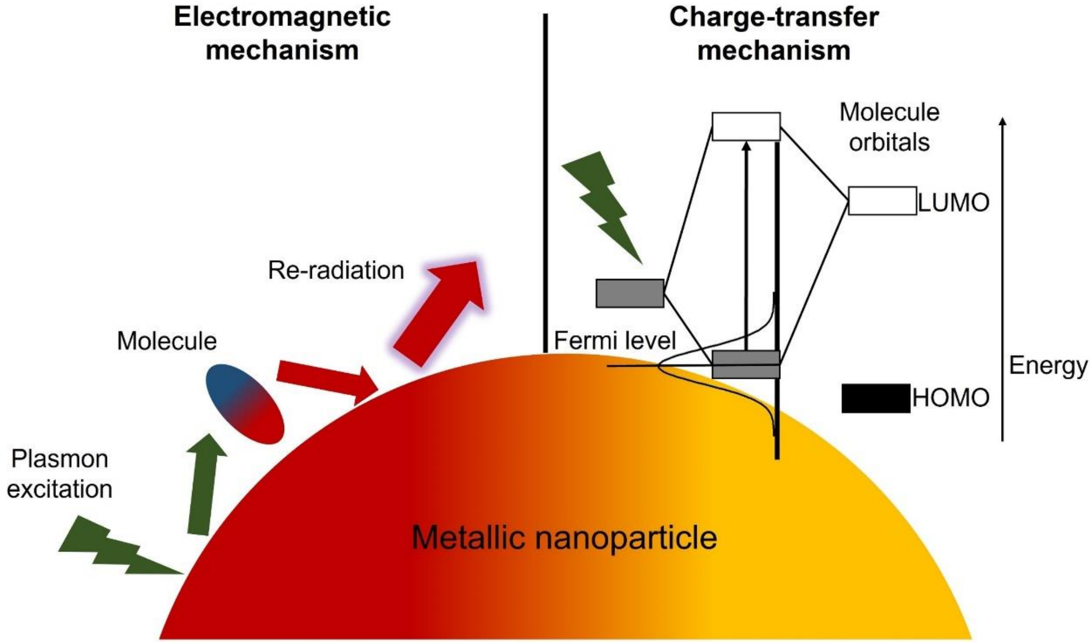

Fig. 4 SERS enhancement mechanisms that occur simultaneously at the nanoparticle surface and surroundings.

On the other hand, in the electromagnetic mechanism, the formation of plasmons around and between the nanoparticles, along with the near-field properties of the metallic nanoparticles, lead to the formation of hot-spots, or areas in which the local electromagnetic field is highly increased due to a high electron density [11], as illustrated in Fig. 5. When a probe molecule is in a hot-spot, the Raman signal produced is highly enhanced due to the local electromagnetic field influence, as the nanostructures act as nanoantennas that amplify the signal by a re-radiation process, leading to intensity enhancements as high as 10^7 or even higher. However, such increases are commonly reached when the particles contained in the nanostructured substrate have an anisotropic morphology, a high roughness, or sharp edges or peaks, such as nanostars, nanocubes, nanoprisms, nanodendrites, and several other morphologies [20].

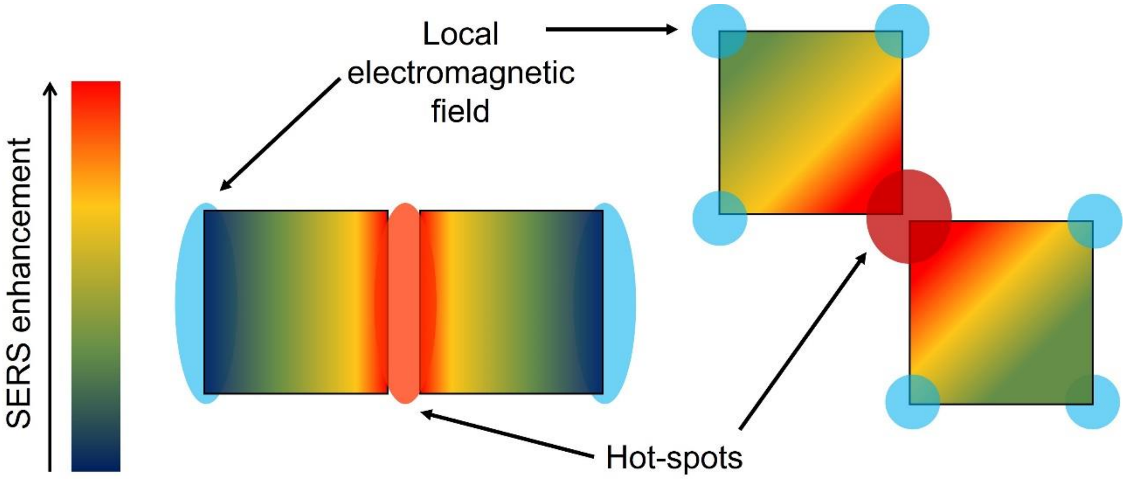

Fig. 5 Representation of hot-spots produced by the interaction between the plasmon modes of two or more nanostructures.

Nevertheless, to achieve such enhancements, the nanostructures must be close enough between them to form hot-spots, this is hard to reach by using mild deposition procedures; therefore, the procedures mainly used to fabricate SERS substrates consist in the use of techniques such as lithography, electrospinning, chemical synthesis, self-assembly, etching, among others [21-23]. Although the production cost is usually high, their reproducibility is higher than the one reached by mild deposition methods. Due to this, researchers are looking for new ways to fabricate low-cost SERS substrates with high reproducibility. A recent alternative is the combination of the microfluidic devices and SERS, often referred to as microfluidic SERS (MF-SERS). This variation combines the sensitivity of SERS and the reproducibility of the microfluidic devices, which also allows the use of very low sample volumes (in the order of μL or mL).

1.3 Microfluidics and MF-SERS

The microfluidic devices, also known as Lab-on-a-chip, represent a great advance in modern technology as they can perform several tasks in a small device. Some of the operations that can be performed in a microfluidic chip are mixing, heating, species separation, purifications, preparation of serial dilutions, among others [24-26]. Some examples of microfluidic chips are shown in Fig. 6. An additional advantage of these devices is the fact that they represent the miniaturization of a process, and can be perfectly controlled, allowing, for example, an automatic and miniaturized determination of a sample in real-time as an on-line analysis, which is a feature especially useful during an industrial manufacturing process or a field trip.

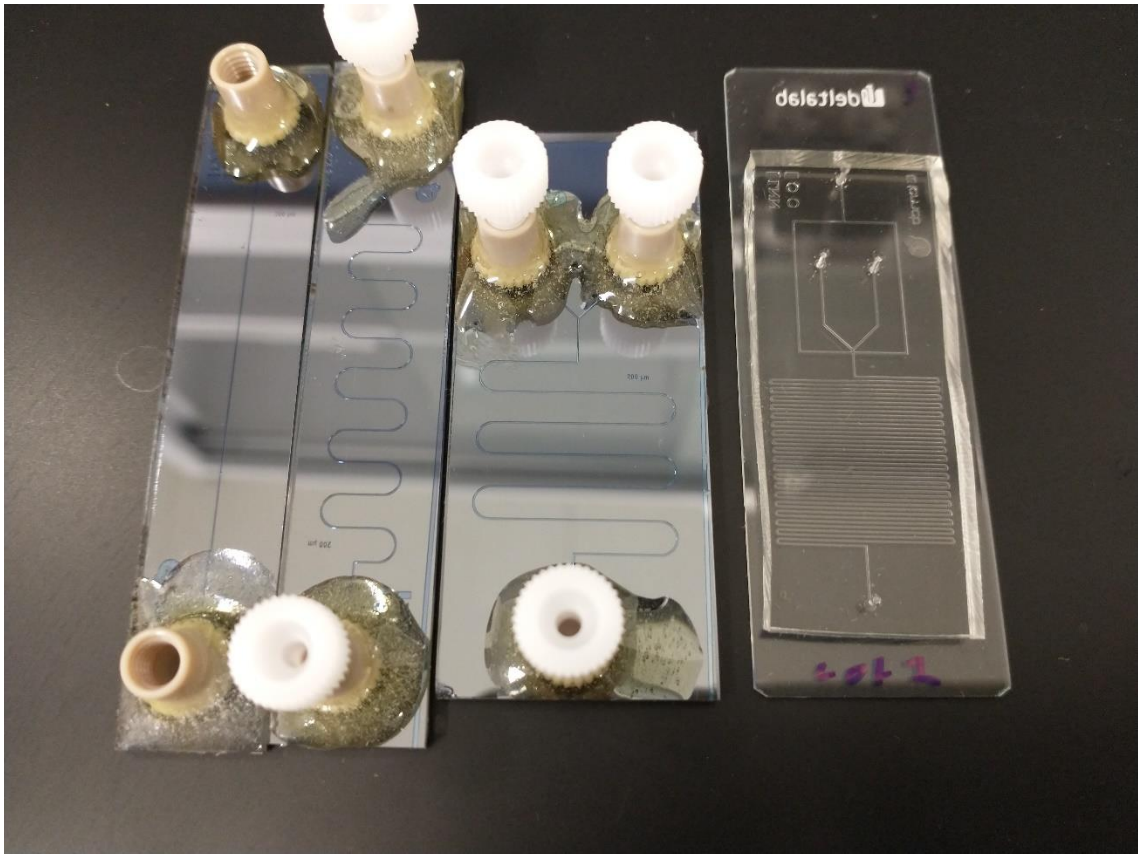

Fig. 6 Examples of microfluidic chips made in silicon wafer and glass-PDMS.

By combining SERS with microfluidics, we obtain a technique that solves some of the problems normally presented in SERS such as avoiding the sample bleaching caused by irradiating the sample for a long time with an energetic laser, this is solved due to the low energy collection as the sample flows through the microchannels [27]; also, a faster and more reproducible analysis can be performed using less amount of the sample [28,29]; the sample can be pre-treated *in situ* inside of the chip itself, a few seconds before the analysis [30]; as it is a dynamic technique, no sub-reactions are produced by the focused laser [27,31]; among others. Fig. 7 shows some microfluidic chip designs for SERS analysis.

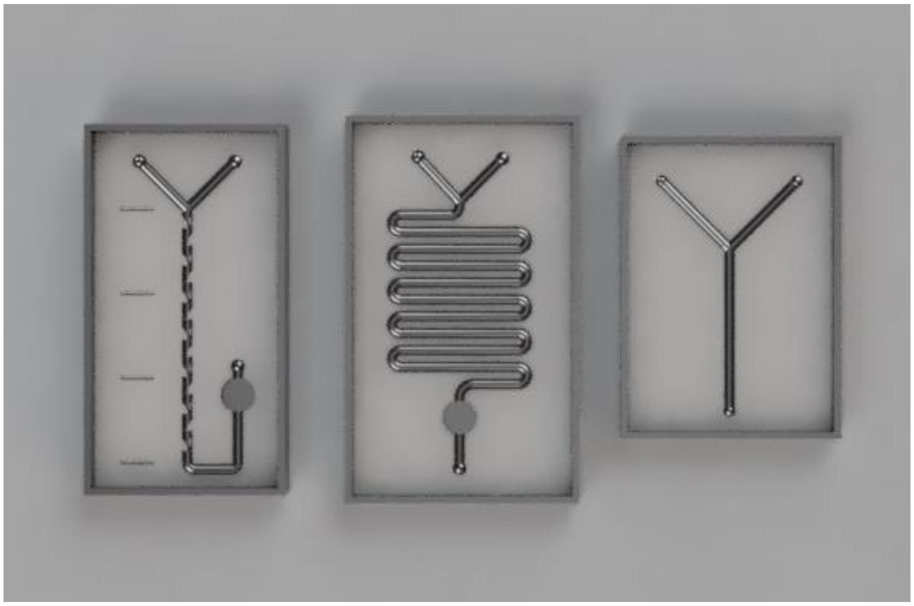

Fig. 7 Microfluidic chip designs for SERS analysis.

Nevertheless, the MF-SERS analysis is limited by the capability of the research group to synthesize the active nanostructures that will be inside of the microchannels, whether before the addition of the chip lid [32,33] or after the lid adhesion (usually by laser lithography or pre-treatment of the microchannels themselves) [34,35]. Another way to perform a MF-SERS analysis is by premixing the nanoparticles and the sample before their injection into the chip [36]; or by the injection of both, the sample, and the nanoparticle dispersion, into the chip and allow them to mix before they reach the analysis area of the chip [37]. In any way, these cases show the flexibility of the technique.

On the other hand, a problem with the microfluidic devices is their fabrication due to the high sensitivity needed to form such small channels. The most common procedure for the fabrication of substrates is based on the drawing of the microchannels on a Si wafer by soft lithography, using it as a master mold for the obtainment of a polydimethylsiloxane (PDMS) substrate that contains the microchannels, a process followed by its surface treatment to allow its adhesion with a glass lid or cover [38]. Nevertheless, other procedures have been reported, such as glass etching with HF to form the microchannels [39]. As it can be observed, the formation of microfluidic channels often requires the use of specialized techniques and reagents (such as photomasks, etching agents, etc.). Due to this, new and cost-effective methods for the formation of precise microfluidic channels are required to open the use of this technique to non-trained personal, industrial laboratories, and quality control departments, just to mention a few areas that will benefit from lowering the cost of consumables and analyses related with the MF-SERS technique.

Talking about the physical features of a MF-SERS chip or substrate, its size may vary depending on its manufacture process and the number of processes it can develop, even some have multi "floor" or level architecture, allowing even more processes and retention time when required. Even though this kind of products are often fabricated in PDMS and glass as mentioned, acrylic is also a suitable substrate for chips fabrication, as well as paper microfluidics (often known as later flow tests), in which different structures of paper are built in to take advantage of the capillary effect and thus avoid the need of pumps and tubbing. Similar devices can be constructed in any other material by taking advantage of the microchannel diameter and thus designing built-in capillary pumps and filters, in such chips, the inlet is an open structure where a drop of the sample can be placed to start to flow through the substrate.

The latter demonstrates how important the chip design is, as it must consider the processes that will occur, the chemical compatibility between samples, reagents, and the chip itself, as well as the microchannels length required to ensure an efficient mixing. Even though most of the microfluidic chips contain channels in the order of 100 to 200 μm of diameter, some others contain channels as wide as 500, 700 or even 1000 μm, reaching the so called millimetric fluidics. At this point, the channel diameter has a direct impact on the most suitable channel length. This is due to the relationship between the inertial and the viscous forces at such small scale, which then causes the flow to undergo in a laminar or turbulent regime. In this case, as the channels are usually at the micrometric scale, the flow is usually at a laminar regime, in which all the flows run parallel from each other, and thus, little or no mixing occurs. In this case, incorporating mixing structures in the channels, and increasing the channels length, are two of the most common alternatives to allow the diffusion and mixing of the flows, which represents a vital step to adequately perform all of the other processes.

1.4 3D printing

3D printing is usually referred to as a manufacturing procedure in which a material is extruded in layers to form a complete 3D object; nevertheless, this concept refers to a series of methods and techniques that forms an object by a layer-by-layer approach, also known as additive manufacturing. Even though this is not new, the possibility to produce any personalized object in hours or even minutes is rapidly becoming popular throughout the whole world, even for non-trained people.

As mentioned, additive manufacturing englobes seven main manufacturing processes: vat photopolymerization, material extrusion, sheet lamination, powder bed fusion, binder jetting, material jetting, and directed energy deposition. Each of these processes has its advantages and disadvantages, as well as their specific materials and mechanical properties. Among these seven techniques, vat photopolymerization (also known as stereolithography or SLA) and material extrusion (which is the technique directly related to the “3D printing” term) are the most popular additive manufacturing methods with a non-industrial approach, even though they are used by many different industries.

In the case of SLA, a photosensitive or photocurable material is used as the main component. This material is usually composed of epoxy- or acrylate-based resins; however, any photocurable material can be used as long as it is in a liquid state. To form the object, a laser contained in the equipment is focused on a vat or container filled with resin and as it interacts with this material, it solidifies, forming the product layer after layer.

On the other hand, the material extrusion procedure is based on the capability of the 3D printer to melt a filament and extrude or “push” it onto a heated bed following the instructions contained in the g-code file to form the object, as shown in Fig. 8. In this technique, any material that can be completely melted in the temperature range of the equipment is a potential printing material; nevertheless, the most common are ABS (acrylonitrile butadiene styrene), PLA (polylactic acid), PET (polyethylene terephthalate), nylon, among others.

3D printing is a very useful technique for laboratories that are constantly improving their materials, as it can be used for fast prototyping, customizing laboratory materials such as reaction containers or cells, devices manufacturing, production of controlled enclosures, just to mention a few cases.

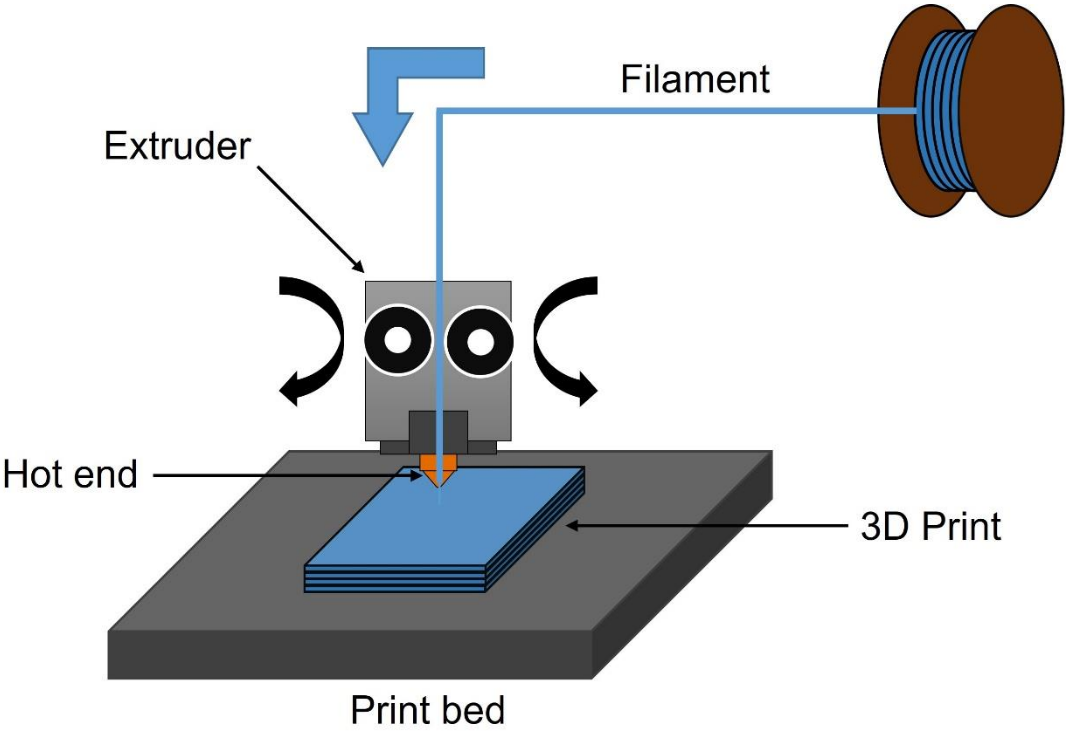

Fig. 8 Scheme of an extrusion 3d printer, that pushes a plastic filament through a hot end and nozzle to 3D print an object layer by layer.

There are different parameters that must be considered to obtain an accurate and useful print, starting from the 3D model design. This design constructed usually using a specialized software must be accurate according to the dimensions required and measured, and then it can be converted into a standard triangle language (STL) file by the software, to be modified in a “slicer” program. In the slicer, the physical printing parameters are manipulated to a desired profile, infill, supporting and adhesion structures, and even special features that may ease the print. Talking about each one of them, profile or layer height has a direct impact on the product resolution; infill is a measurement of how solid the product will be (in percentage); the supporting structures are aids on printing parts that have no structural parts and may fall apart due to gravity, such as the middle part of a bridge-like product. Lastly, the adhesion structures help on the correct first layer adhesion, which has a great importance on avoiding printing defects.

Even though we can control almost every aspect of the printing process through the slicer, the real performance of the printing process is dictated by the machine. In this aspect, many parameters must be considered as well: correct storage of the filament, choosing a material suitable for our requirements (chemical resistance, higher thermal or mechanical properties, flexibility, etc.), setting a nozzle that allows the resolution needed, leveling the printing bed, among many others that must be known and controlled by the operator.

Post-processing is an additional step required in some uses, such as those that involve the containment of water or any other liquid such as molding resins. In this case, the print may undergo different processes to grant a smooth finish and get rid of any imperfections or holes in the solid body, such as acetone vapor smoothing (used only for ABS), and sanding, priming, and finishing.

Due to the latter stated, in this project, we purpose the synthesis of Ag nanostructures with different morphologies and their use to fabricate microfluidic chips for SERS, using 3D-printing and shrinkable polymers as master molds, to obtain a cost-effective platform for the reproducible analysis of samples in low volumes by MF-SERS.

CHAPTER 2

2.1 Background

Several methods for the production and characterization of plasmonic nanostructures have been reported along the years, some of them focus on the analysis of a given factor such as the concentration of any of the reagents and its relation to the other species, some other reports investigated the effect of the physical parameters such as temperature, pH, pressure, etc. This is translated as a range of methodologies for the obtainment of nanoparticles with a specific and controlled size, shape, chemical environment, optical properties, polydispersity. Such variety allows us to choose a method and even modify it to obtain a dispersion that suits our requirements.

Table 1 shows a summary of different synthetic procedures reported to produce four Ag nanostructures: nanospheres, nanocubes, triangular nanoplates, and decahedra; in this table, the particle size is mentioned, as this is an important factor that can directly affect the SERS substrate architecture and performance; also, the reducing and stabilizing agents are mentioned, due to their importance on the morphology formation and growth. Lastly, special conditions are also mentioned, as these can finely tune the reaction outcome.

Table 1. Summary of different synthesis methods for the obtainment of Ag nanoparticles with specific morphology.

Morphology	Conditions	Reductor	Stabilizer	Size (nm)	Reference
Spheres	Boiling temperature	Na_3Cit	Na_3Cit	30 – 100	40
	Reductor added dropwise	$NaBH_4$	Na_3Cit	5 – 20	41
	Glycol solutions, 185 °C	Ethylene glycol	PVP	50 – 150	42
Cubes	155 °C	Ethylene glycol	PVP	25 – 350	43
	120 °C in autoclave	Glucose	CTAB	50 – 60	44
	60 °C, pH 3.1, light conditions	Ascorbic acid	CTAC	30 – 100	45
Triangular plates	Use of H_2O_2	$NaBH_4$	PVP-Na_3Cit	30 – 100	46
	Fluorescent light (40 W)	$NaBH_4$	Na_3Cit	70 – 200	47
Decahedra	LED light (465 nm)	$NaBH_4$	PVP-Na_3Cit	30 – 50	48
	LED light (450 nm), arginine, H_2O_2	$NaBH_4$	PVP-Na_3Cit	40 – 170	49

Among the procedures mentioned, we can remark the one reported by Lee & Meisel in 1982 [40]. Even though this method was written long ago, it set the bases of the next syntheses, as they are modifications of this original work. In this paper, the authors use a $AgNO_3$ solution that is then heated until boiling conditions, then, sodium citrate (Na_3Cit) is added and acts as both, reducing and stabilizing agents. It is widely known that this reaction leads to Ag nanospheres (AgNS) with a diameter between 20 and 100 nm, depending on the reagent concentrations and control. The latter case is due to the growth mechanism of the nanoparticles themselves, and this can be directly compared to the dispersion obtained when $NaBH_4$ is used as reductor, such as the case of the work reported by Agnihotri *et al*. [41]. As $NaBH_4$ is a stronger reducing agent compared to Na_3Cit, the reduction of the Ag^+ ions occur faster and leads to a higher Ag nuclei production, and so the nanoparticles obtained are usually more in quantity and smaller in size (often in a range of 5 – 20 nm). The kinetics of each reaction allows us to produce two dispersions with different properties and uses, as the smaller particles, often referred to as nanoseeds, can be used to prepare bigger nanostructures with specific morphology, whereas the bigger spheres can be used for devices preparation or as seeds for even larger architectures.

In the case of the Ag nanocubes (AgNC), the most successful procedures include the use of polyol compounds such as ethylene glycol, as it can be observed in the work reported by Chen and its research group [43]. Nevertheless, this kind of procedure often requires the use of temperatures as high as 150 °C, often reached by an oil or sand bath. The non-uniform heating of the system often leads to dispersions with a wide range of nanoparticles, especially when the stirring is not suitable. The latter often occurs during the polyol procedures.

Even though the use of glycol-containing reagents is very common [50], in 2016, Zhou *et al.* published a paper about the obtainment of AgNC with sharp edges in a water-based system by using cetyltrimethylammonium bromide (CTAC) as a stabilizing agent, ascorbic acid (AA) as reducing agent, and $FeCl_3$ to avoid the formation of twining particles [45]. In this work, the synthesis occurs as a two-step reaction: first, AgCl nanooctahedra are formed; then, a photoreduction process occurs with regular room light, and thus, Ag^0 nuclei are formed close to the octahedra, leading to a change in the chemical equilibrium and their growth as nanocubes. This dispersion was used to fabricate SERS substrates, which, when detecting 1,4-benzenedithiol (BDT), reached an enhancement factor (EF) of 1.34x10^5, and a limit of detection (LOD) of 10^{-6} M.

Talking about triangular Ag nanoprisms (AgNT), this morphology can also be obtained chemically by the growth and shaping of Ag seeds, as reported in 2017 by Zhang *et al.* [51]. In this paper, the authors compare nanoprisms obtained by the growth of small triangular Ag nuclei synthesized using pluronic F127 (a non-ionic copolymer surfactant), with the large nanoprisms obtained by growing PVP-stabilized seeds. These dispersions were also used as SERS substrates to detect 4-mercaptobenzoic acid (4-MBA), reaching an EF between 2.7x10^4 and 3.9x10^5, and a LOD of 10^{-6} M. Additionally, the determination of thiram in soil was also analyzed, reaching a LOD of 9.9 ng/g.

However, the most used procedure for the obtainment of bigger and geometrical nanostructures is the photoconversion of nanoseeds, a procedure mainly used for the obtainment of nanoprisms. In this procedure, a dispersion of nanoseeds containing shaping agents, such as Na_3Cit, is irradiated with light to induce the formation of Ag^+ ions (if not available) that then lead to the growth of the seeds until a final morphology or size is reached. An example is a work reported by Jin, *et al* [47], in which Ag seeds are photoconverted into AgNT by their irradiation with a conventional 40 W fluorescent light. Similarly, Ag nanodecahedra (AgND) are usually obtained by a photoconversion procedure in which nanoseeds are irradiated with blue light with a wavelength usually close to 450 nm. In this case, the light energy and the stabilizer agent or agents lead to decahedra instead of any other common structure such as nanoprisms. The work reported by Zheng, *et al* [48] is an example, in which using a reactor with 465 nm LEDs and Na_3Cit and PVP as stabilizing agents, allowed the growth of seeds into well-defined decahedra with 33 nm as average edge length; the authors also discuss the importance of a cooling step to dissipate the energy produced during the synthesis, as this leads to a wider nanoparticle size distribution.

This first background section emphasizes the importance of the noble metal nanoparticle morphology to properly tune its optical properties, as well as the importance of this tuning for the development of sensitive devices, especially, SERS substrates. In the following section, a few works about microfluidic chip fabrication for MF-SERS will be reviewed.

In 2007, Grimes *et al*. reported the use of “Shrinky-Dink” for the fabrication of microfluidic chips [52]. They emphasize that the use of these shrinkable toys can be used along with a printer to form shrinkable master molds that can later be used to fabricate the PDMS chips. Later in the same year, the research group published a second paper regarding this method [53]. In this paper, the authors focused on the developing of 3D microfluidic devices using the same shrinkable toy, studying the change in the material dimensions, as the polystyrene thermoplastic sheets used shrink in X and Y directions, but grow drastically in Z or height. Also, the authors recommend that when working with the microfluidic channel formation on such shrinkable materials, the residual plastic must be eliminated and not only cut, as it will grow and can cause a deformation in the microchannels that may lead to clogging.

Ten years later, in 2017, Sun and his research group published their work about shrinkable molds for microfluidic chip fabrication [54]. In this case, the publication is a technical note about the procedure they use to avoid the use of photolithography for master molds preparation. The authors assembled a master mold at a millimeter scale, poured polyurethane (PU), and after its solidification, the solvent evaporation leads to a uniform shrinkage in the 3 dimensions, avoiding deformation; however, the solvent evaporation must be complete to get a replica. Thus, the authors use this PU mold as a new master mold that can be used to get the PDMS chips. For this, they propose a casting-shrinkage cycle to obtain a chip with micrometric channels; most of the time, only two complete PU cycles are required for this.

About the MF-SERS analysis, Popp and his research group reported in 2007 a procedure for the detection of crystal violet (CV) using a microfluidic device combined with SERS [55]. In this work, the authors fabricated a microfluidic chip using glass as a substrate, in which the microfluidic channels were made by HF etching. This chip was used to detect CV, reaching a LOD of 10^{-7} M when measuring by a segmented approach, in which the sample is contained inside of a droplet surrounded by oil, eliminating the memory effect (also known as the deposition of the sample or the nanoparticles onto the microchannels, causing erroneous analysis and changing the real flow). On the other hand, although the authors mentioned the use of this device for on-line measurements, this capability is not analyzed or mentioned in the paper itself. Nevertheless, the idea of incorporating a microfluidic analytical device for on-line characterizations in liquid chromatography with high reproducibility and sensitivity is a promising alternative and tool that merits extensive research.

On the other hand, Yan *et al.* reported in 2017 the fabrication of MF-SERS chips involving the growth of 3D Ag nanostructures by a two-step laser procedure [56]. For this, the authors made a master mold using the standard soft lithography, which involves the use of a photomask and a laser to “write” the microchannels; afterwards, this mold was used to obtain a PDMS substrate containing the microchannels, which was then covered with a glass slide. To form the SERS-active area, $AgNO_3$ and Na_3Cit were injected and irradiated with a laser at a specific area, then a washing flow was injected, and a second irradiation was performed. The authors noticed that after the first irradiation, 3D Ag nanostructures are formed; however, after the second irradiation, the structures are decorated with AgNS, increasing the roughness, and leading to better detecting properties (higher sensitivity). These chips were used for the determination of CV, Nile blue, hemoglobin, and 5-fluorouracil, reaching a LOD of 10^{-13} M; nevertheless, the reproducibility of the technique reduces dramatically at concentrations lower than 10^{-7} M, having a maximum of 50% of detection probability when using 10^{-13} M.

Lastly, Wu and his research group reported a lift-off lithography approach for the fabrication of MF-SERS chips in 2018 [57]. To accomplish this, gold nanospheres were self-assembled onto a (3-aminopropyl)triethoxysilane (APTMS) treated glass, then a PDMS slice containing microchannels was adhered onto the glass and removed to lift off some of the nanoparticles, leaving a specific design on the glass. After this procedure, another PDMS substrate is adhered to the glass to form the final chip. This chip was used to detect Nile blue and ochratoxin A (OTA) fragments; however, it requires the incubation of the sample in the SERS-active area for 1-5 h before its analysis. This work allowed a LOD of 10^{-4} M for Nile blue and 500×10^{-9} M for OTA.

After the literature analysis, we noticed the existence of several reports about the synthesis and characterization of Ag with different morphologies, most of the time by more than one procedure; this helps in the work of preparing optically tuned nanodevices for specific applications such as SERS. Also, it is observed that the use of anisotropic shapes, especially tips or peaks-containing morphologies, lead to a high local electromagnetic field enhancement, which is directly connected with the device capability of sensing probes at low concentrations; thus, making the particle morphology an important factor for the sensitivity variation.

On the other hand, there are just a few works regarding the fabrication of microfluidic devices by using shrinkable plastics, whether to obtain a master mold or to build the apparatus itself; in these cases, polystyrene thermoplastic and shrinkable PU are the polymers employed. In the area of MF-SERS, it can be observed that most of the reports require the use of soft lithography for the fabrication of the microchannel-containing master mold, which involves special laboratory infrastructure and materials (such as Si wafers, photomasks, etc.) and requires time and carefulness to obtain usable chips without clogging. Similarly, the MF-SERS analysis can be performed in two ways: injecting a pre-synthesized dispersion that will then be mixed with the sample or making the Raman probe interact with *in situ* grown nanostructures. In any of the two ways, the particles used usually present a spherical shape, meaning that the effect of the morphology has not yet been reported nor meticulously studied. Lastly, in some of the analysis protocols reported, the sample incubation for some hours must occur to be able to detect the probe, this eliminates the actual advantage of the microfluidics itself: a dynamic analysis with a potential to be applied on-line in any manufacturing facility.

2.2 Hypothesis

Ag nanostructures with different morphologies allow the on-line determination of *p*-aminothiophenol at a concentration of 10^{-9} M by microfluidic surface-enhanced Raman spectroscopy.

2.3 General objective

To synthesize and characterize Ag nanostructures with specific morphologies, use them to fabricate PDMS-glass microfluidic chips, and to evaluate their performance in on-line SERS.

2.4 Specific objectives

- To synthesize Ag nanoparticles with different morphologies (AgNS, AgND, and AgNT).
- To characterize the noble metal nanoparticles by optical (UV-Vis spectrophotometry), and microscopic techniques (scanning and transmission electron microscopies).
- To design and fabricate PDMS-glass chips for microfluidic SERS by using 3D-printing and polyurethane shrinking master molds.
- To deposit nanostructures into the microfluidic channels by surface functionalization and nanoparticle autoassemble.
- To characterize the nanostructure-containing microfluidic channels by Raman spectroscopy.
- To determine the best flow conditions required to perform SERS analyses.
- To evaluate the SERS performance of the microfluidic chips when used as SERS substrates.

- To determine the analytical limit of detection of the chips by microfluidic SERS and a suitable Raman probe.

CHAPTER 3

MATERIALS AND METHODS

3.1 Materials

Trisodium citrate (Na_3Cit), silver nitrate ($AgNO_3$), sodium borohydride ($NaBH_4$), *p*-aminothiophenol (*p*-ATP), (3-mercaptopropyl)trimethoxysilane (MPTMS), and chloroform ($CHCl_3$) were of reagent grade and purchased from Sigma-Aldrich (Toluca, Estado de México, Mexico), deionized water was used to prepare solutions, polyurethane (Hydrospan 400) was purchased from Industrial Polymers Corporation (Houston, Texas, United States), and polydimethylsiloxane (PDMS, Sylgard 184) silicone elastomer base and curing agent (Dow, Wiesbaden, Germany).

3.2 Synthesis of AgNS

AgNS dispersions were obtained using the Lee & Meisel synthetic method [40], as this procedure leads to nanoparticles bigger than 10 nm. In a regular synthesis, 20 mL of 1 mM $AgNO_3$ were heated until boiling, then, 400 μL of a 1% w/v Na_3Cit solution were added in one step and let react for 10 min in the absence of light to avoid side photoreactions. The dispersion color changed from colorless to orange-green. The dispersions were purified and washed by centrifugation at 4000 rpm for 20 min, followed by its redispersion and storage for its further use.

3.3 Synthesis of AgNT and AgND

To grow AgNT and AgND dispersions, Ag nanoseeds were first synthesized by a protocol reported by our research group [58]. In this protocol, 58 mL of distilled water is mixed with 30 mL of 5 mM Na_3Cit and 10 mL of 1 mM $AgNO_3$. As a final step, 2 mL of 8 mM $NaBH_4$ are added dropwise while stirring to ensure a quick formation of small spherical nanoparticles. In this method, the molar relation between $AgNO_3$ and Na_3Cit is 1:15 to ensure enough stabilizer molecules to shape the particles.

As a second step, the previously obtained dispersion is then directly exposed to light. In this case, an RGB LED photoreactor was built to grant us complete control on the light wavelength applied. In a regular synthesis, the nanoseeds obtained are poured into test tubes, which are then set into a water-containing beaker inside of the photoreactor. The tubes are then irradiated for 24 to 48 h, depending on the wanted shape: for AgNT, green light is irradiated for 48 h, whereas for AgND, blue light is used for 24 h. For the nanoparticle purification, the dispersions were centrifuged at 6000 rpm for 20 min, washed and redispersed in distilled water, and stored for their use. The LED chips wavelength ranges are 620 – 630 nm for red light, 520 – 530 nm for green light, and 465 – 475 nm for blue light.

3.4 Characterization of the noble metal nanostructures

The Ag nanostructures were characterized through UV-Vis spectrophotometry to determine their optical properties, and to determine their size and shape, the dispersions were also characterized by field-emission scanning electron microscopy (FE-SEM) using a FEI Nova NanoSEM 200 microscope, and by transmission electron microscopy (TEM) using a JEOL JEM 2200FS microscope.

3.5 Microfluidic chips fabrication

First, microfluidic chip molds were designed in a 3D-design specialized software and printed. Then, a PU – water mixture at a 1:4 volume ratio was poured into the chip mold and let cure. The cured mold was then removed and dried at 60 °C for 46 h to let the material shrink. With this master mold, a mixture of PDMS pre-polymer and curing agent in a 10:1 weight ratio is poured into a Petri dish containing the master mold, degassed with a vacuum chamber until no bubbles are trapped nor formed, then cured in an oven at 70 °C for 2 h. Afterwards, the solid PDMS chips were cut, the inlets and outlets punched, and lastly, the chips were covered with tape to avoid any material to clog the microchannels. The PDMS chips and glass slides were cleaned with isopropanol and plasma treated for 1 min, then the chips were assembled by quickly bonding a PDMS substrate with a glass slide, pressed together and heated at 70 °C for 2.5 h. To decorate the chips with nanostructures, the microchannels will be flooded with a nanoparticle paste and dry overnight in an oven at 60 °C.

To fabricate acrylic microfluidic chips by a micromilling process, 1.3 mm thick acrylic sheets were carved using a MDX-40A Roland AG milling machine with 200 and 800 μm square end drill bits (Kyocera, 1600-0080L012 and 1600-0320L48) at 11000 rpm speed, and 1 mm/s feed rate, allowing the fabrication of 200 μm microchannels in one sheet and 800 μm inlets and outlets in a second sheet. After both parts were fabricated, they were exposed to $CHCl_3$ vapor for 1 min in a closed Petri dish, which attacked the surface of both acrylic sheets, allowing the sealing of the microchip by clamping both sheets together at 90 °C and 250 psi for 5 min. The decoration of the microchannels with nanoparticles was carried out by flooding using a nanoparticle paste and drying at 60 °C overnight.

3.6 MF-SERS measurements

For the sample analysis, a *p*-ATP solution will be injected into the microfluidic chip through a plastic tube inlet, forming a continuous sample flux; during this flux, the nanoparticle-decorated microchannels will be focused and analyzed. The outlet of the chip led to a collector beaker to ensure its correct disposal. For a preliminary analysis, 1 mM *p*-ATP will be used; however, after the microfluidic study analysis is standardized, LOD determination study will be carried out using a range of concentrations between 10^{-3} and 10^{-12} M for each SERS microfluidic substrate. The Raman equipment used for this work will be a Thermo Fisher Scientific DXR Raman microscope with a 780 nm laser at a power of 12 mW using a 50X objective and an integration time of 1 s.

CHAPTER 4

RESULTS AND DISCUSSION

4.1 Nanoparticle characterization

4.1.1 Silver nanospheres (AgNS)

AgNS dispersions were prepared by the Lee & Meisel method as stated in the previous section; this allows us to obtain nanoparticles with diameters higher than 20 nm, which will then lead to the creation of hot-spots with higher electromagnetic field change than those created when nanospheres with diameters close to 10 nm are used. As the hot-spots on SERS substrates are formed when two or more plasmonic nanoobjects interact, and as the effect of the hot-spots themselves on the local electromagnetic field is produced by the interaction of the peaks or small areas of the nanoparticles, then a higher size gradient will lead to a higher effect. This can be imaged when we compare two different systems: the interaction between two small spheres, and between two bigger spheres. The size gradient of the first case is small, as the “hole” formed in between the two small spheres has a low deepness compared to the one produced when two bigger spheres interact. In this analogy, the hole is the area where the hot-spots can be produced when the plasmonic modes of the nanospheres interact. This hot area is where the Raman intensities can be highly amplified by the re-radiation process, and thus, is where we need to locate the Raman probe molecules to ensure a higher signal recognition. Due to the latter, using nanospheres bigger than 10 nm is a promising method to ensure better SERS responses.

In Fig. 9, the UV-Vis spectrum of the obtained AgNS dispersion is shown. In this spectrum, a maximum absorption band can be observed close to 425 nm, which can be associated with the LSPR of spherical Ag nanoparticles. Similarly, a second absorption band is shown at 545 nm as a growing shoulder signal, which can be associated with a quadrupolar plasmon mode [59,60].

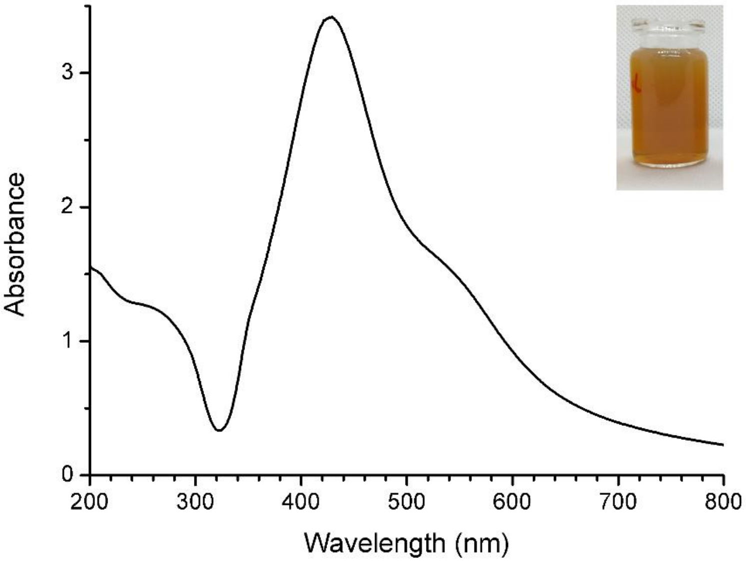

Fig. 9 UV-Vis spectrum of the AgNS dispersion. The inset shows a photo of the dispersion.

If we were to compare this dispersion with a Ag nanoseed dispersion (with an average size of 7 nm), we will observe some differences as the ones shown in Fig. 10. In this figure, the UV-Vis spectra of both Ag dispersions are shown, as well as photographs of both systems. The first difference that we can mention is the color of the dispersion itself, whereas the AgNS dispersion is orange-green, the Ag nanoseed system shows a yellow color; this has a direct link to their UV-Vis spectra, as the AgNS spectrum shows two absorption bands, product of two plasmonic modes, whereas the Ag nanoseed shows only the main dipolar mode at 415 nm.

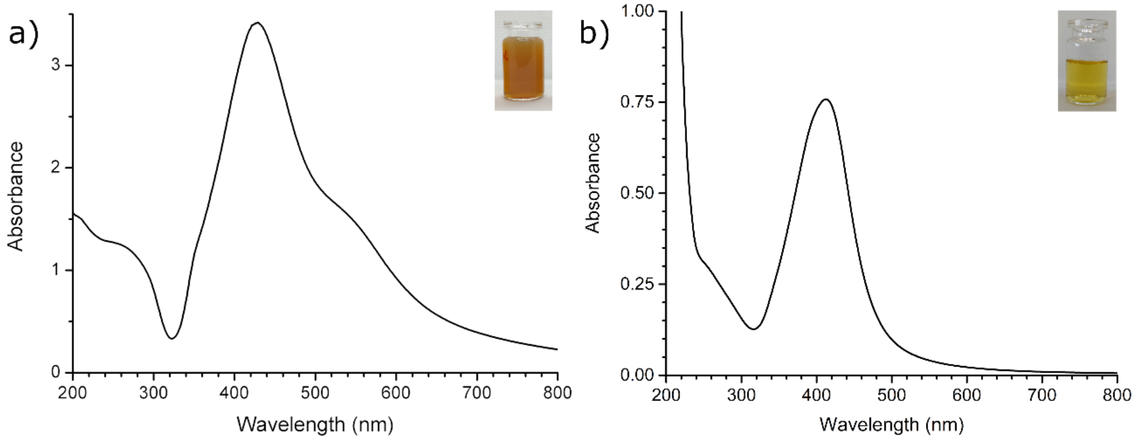

Fig. 10 UV-Vis spectra and photographs as insets of: a) AgNS dispersion obtained by the Lee & Meisel protocol, and b) Ag nanoseeds dispersion.

This difference can be explained by studying their synthesis procedures and growth mechanisms. The main experimental difference between both protocols is the used reducing agent, which can be Na_3Cit or $NaBH_4$. $NaBH_4$ is known as a powerful reducing agent, leading to fast reactions; nevertheless, to allow the formation of nanoparticles, it must be added slowly in stirring conditions. On the other hand, Na_3Cit requires energy and time to reduce the Ag^+ to Ag^0. Talking about the nanoparticle growth mechanisms, it is known that the use of $NaBH_4$ leads to fast Ag^+ reduction and nuclei formation which will then undergo two coalescence phases divided by a metastable state; this mechanism produces Ag nanoparticles with a spherical-like shape with a fast kinetics, and thus, the particles are small in diameter, often between 5 and 15 nm; lastly, a UV-Vis analysis of this dispersion usually shows an absorption band close to 410 nm [61]. On the other hand, by using Na_3Cit as reducing agent, the Ag^+ are reduced to Ag^0 and then a series of citrate-containing complex compounds are formed; as a second step, these species undergo aggregation and form small nanoclusters which then form Ag nanoseeds. Thanks to the Ostwald ripening stage, the Ag^+ ions that are free in the system are incorporated onto the nanoseeds, leading to their growth until the final AgNS are obtained. As it can be observed, this process is slower than the $NaBH_4$-reduced mechanism, leading to nanoparticles with a bigger diameter. Also, by the UV-Vis characterization of this dispersion, the main LSPR peak can be observed close to 420 nm [62].

If we compare both spectra shown in Fig. 10, we can observe that the wavelength of the maximum absorption bands are 425 nm for the AgNS produced by a Na_3Cit reduction, and 415 nm for the Ag nanoseeds obtained by using $NaBH_4$; this corresponds to the spectra characteristics that can be predicted to the growth mechanisms mentioned. Nevertheless, we can observe other differences: the AgNS spectrum has two absorption bands.

As it was mentioned in this work, the citrate-reduced nanoparticles undergo a slower growth mechanism, which leads to the formation of bigger nanospheres; also, we know that the dispersion properties are directly affected by the general morphology of the nanoparticles. There are experimental and simulation works that reported that as the size of Ag nanoparticles increases, their LSPR modes change as well, directly impacting their properties [59,60]. In the case of the Ag nanospheres, a second absorption band is formed as the size increases; this band is associated with the formation of a quadrupolar LSPR mode; thus, the presence of this band in the AgNS spectrum is an indication of the obtainment of nanospheres with a bigger diameter. As the 545 nm band has a lower absorbance than the 425 nm plasmon, it could mean that the dispersion is still under the growth step; this can be analyzed by performing a reaction kinetics analysis at different reaction times.

To confirm the latter stated, FE-SEM analysis was performed, and the micrograph obtained is shown in Fig 11. In this figure, particles with a spherical shape can be observed as an agglomerated structure; the particles show an average diameter of 40.4 ± 1.6 nm, which confirms the obtainment of bigger particles than those obtained by using $NaBH_4$ as reducing agent, as suggested by the UV-Vis spectra evidence. This analysis also allowed us to notice that some organic matter (Na_3Cit remnants) is still in the dispersion, which indicates the difficulty of purifying this kind of dispersion. Also, TEM analysis was performed to be able to properly observe the obtained nanostructures. This micrograph, shown in Fig. 12, allow us to better observe and measure the Ag particles, in this case, the resolution of the microscope allow us to measure an average diameter of 38.7 ± 1.9 nm. Also, rod-like shapes can be observed as well in the dispersion, indicating that there is a small contribution of this morphology in the overall optical properties of the dispersion, yet a thorough centrifugation might ensure a higher purification of this dispersion.

As the AgNS synthesis procedure uses Na_3Cit as reducing and stabilizing agent, its concentration is an important factor that might impact the size, shape, and concentration of the nanospheres; thus, a study of the effect of the citrate concentration was performed. In Fig. 13, the UV-Vis spectra of the AgNS dispersions obtained by using five Na_3Cit concentrations are shown; it must be indicated that the dispersions were prepared using a 1% w/v Na_3Cit stock, reaching the following final citrate concentrations: 0.38, 0.76, 1.13, 1.49, and 1.85 mM by using 200, 400, 600, 800, and 1000 μL of the stock solution, respectively. Also, a photograph of the obtained dispersions is shown in Fig. 14.

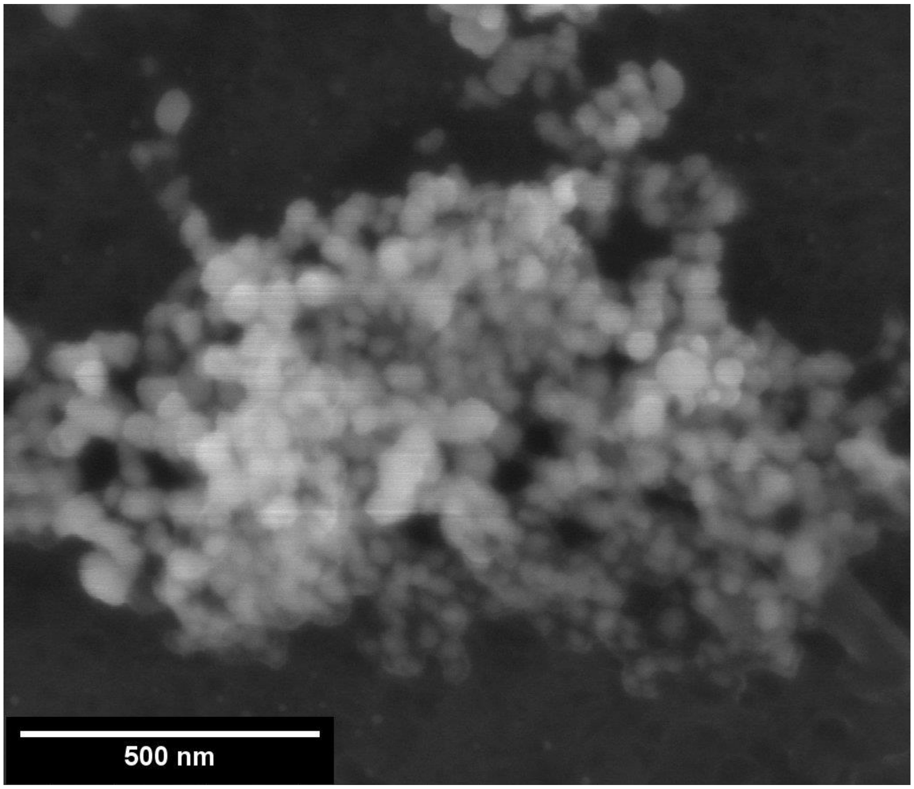

Fig. 11 FE-SEM micrograph of the AgNS dispersion.

As it can be observed in Fig 13, the UV-Vis spectra are similar, yet, as the citrate concentration increases, the absorbance increases as well; this can be explained by the formation of more nanospheres as additional citrate molecules are available by increasing its concentration. The shape of the spectrum shows no changes, indicating that no additional morphologies are obtained. However, experimentally, as the citrate concentration increased, the amount of Ag deposited onto the beaker walls increases as well. A possible explanation of the latter is that, as the AgNS concentration increases, the interactions between the nanoparticles and the energy applied as heat led to local unstable areas, where the particles got deposited onto the walls to lose energy and become stable. This issue makes the Ag concentration hard to control, as the final system is more diluted than expected. For this reason, we decided to use 400 μL of the Na_3Cit stock (final concentration of 0.76 mM), as it showed a good and clean UV-Vis spectrum, and the dispersion shows the same color as the ones obtained with a more concentrated solution as shown in Fig. 14, yet the amount of Ag lost by wall deposition is minimum.

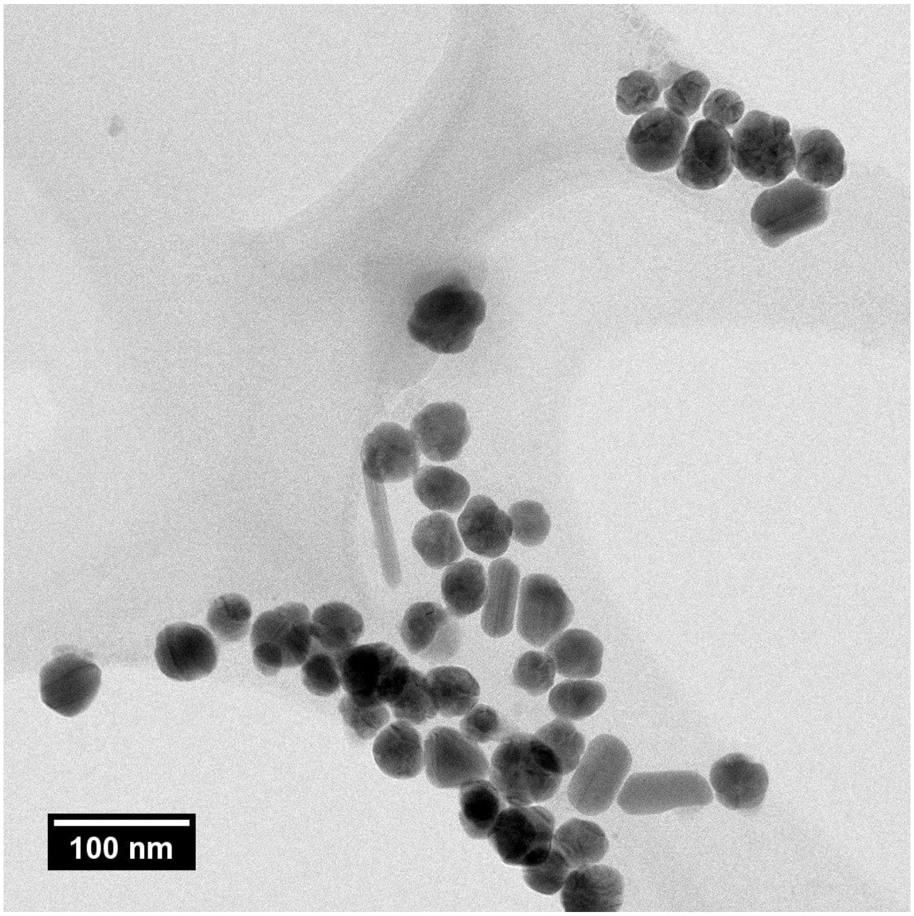

Fig. 12 TEM micrograph of the AgNS dispersion.

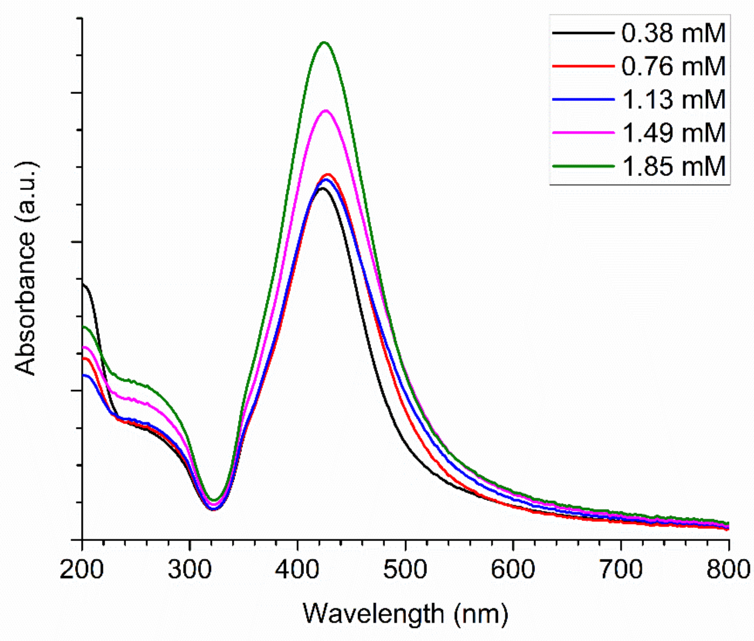

Fig. 13 UV-Vis spectra of the AgNS dispersions obtained using different Na_3Cit concentrations.

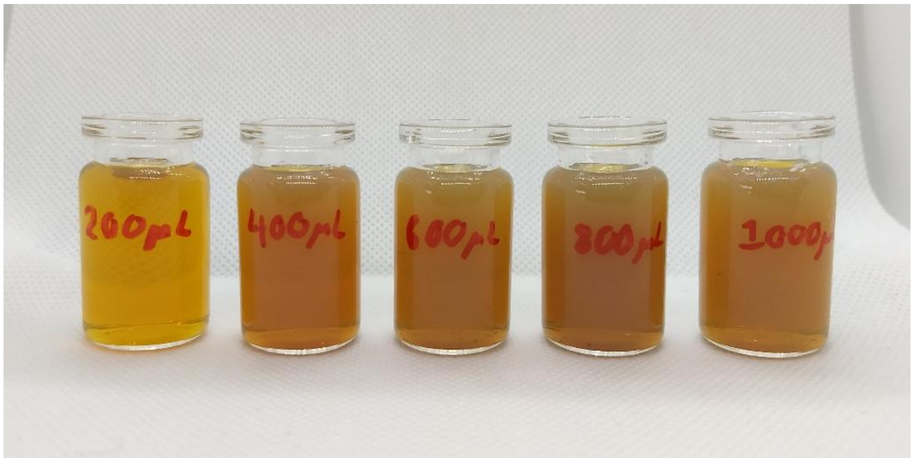

Fig. 14 Photographs of the AgNS dispersions prepared using different Na_3Cit concentrations. From left to right: 0.38, 0.76, 1.13, 1.49, and 1.85 mM.

4.1.2 Silver triangular nanoplates (AgNT) and nanodecahedra (AgND)

As stated before, the obtainment of nanoparticle with complex morphologies such as pyramids, prisms or plates, stars, etc., is usually reached by using a single-step complex synthesis, or by the growth of lower shapes, such as spheres or nanoseeds. In the case of the obtainment of Ag nanoplates, the use of light for the photoconversion of nanoseeds is a good alternative that requires no additional reagents. Fluorescent light is usually the main equipment required for the light-induced growth of nanoseeds into higher shapes. In this work, we used a simple 3D printed photoreactor that works with an RGB LED lights strip to ensure a narrower wavelength range as well as cold light that does not drastically heat the dispersion, as this is an external factor that can affect the outcome.

As a first approach, the AgNS dispersion was set into test tubes in a beaker filled with water, then the LED lights were set to blue color and the dispersion was left to react for 4 days. After 4 days, no change in the dispersions was observed. As a next approach, the pH of the dispersion was changed, as the chemical environment of the system can change the interactions between the chemical species.

For the pH effect study, AgNS were obtained following the reported conditions; nevertheless, the pH of the final dispersion was adjusted with NaOH or HCl, according to the objective value, reaching values of 2.8, 4.5, 5.5, 6.5, 7.5, 8.5, 9.5, and 11.4. As the pH became highly alkaline or acidic, the dispersion changed due to the destabilization of the particles and the formation of other components. For the rest of the experiments, the dispersion did not show any change. The nanoparticles were set under photoconversion conditions: blue light for 2 days, in a water-filled beaker. After the procedure, the nanoparticle dispersions showed some precipitation; however, the color remained unchanged. Fig. 15 shows the UV-Vis spectra of the dispersions at pH values of 2.8, 6.5, 7.5, and 11.4 after the photoconversion procedure.

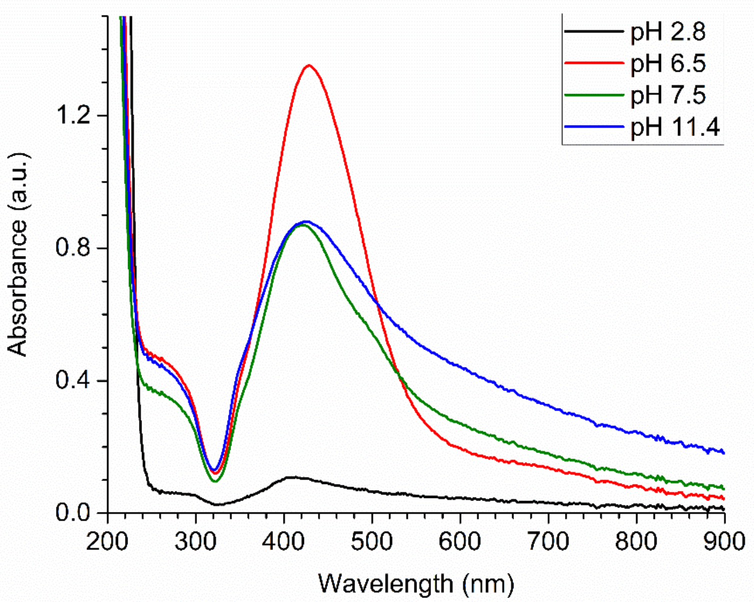

Fig. 15 UV-Vis spectra of AgNS at different pH values after photoconversion for 2 days at blue light.

As it can be observed in Fig. 15, the UV-Vis spectra of the pH-modified dispersions show the signals of a regular AgNS dispersion; however, the absorbance varies depending on the pH, showing the highest for the one with a pH of 6.5, which are the unchanged nanoparticles. This is caused due to the change in the chemical species in the system, leading to precipitation in some cases, just as in the 2.8 and 11.4 cases. It must be mentioned that as the spectra showed the same absorption bands as a normal synthesis before the photoconversion, then no additional shapes were formed during the photochemical procedure.

After studying the pH effect, we worked on the citrate ions concentration and availability before the photoconversion. The citrate ions are a shaping agent, their presence in the system is important to obtain triangular nanoplates instead of hexagonal nanoplates or any other morphology. For this study, we tested three systems: the normal AgNS dispersion; a dispersion obtained by the same procedure, however using a 0.75 M

Na_3Cit stock solution; and a third system made by adding Na_3Cit powder after the normal AgNS formation. These two modified dispersions were designed to have a Ag^+ - citrate ions concentrations relation of 1:15, which will increase the number of available citrate ions. Nevertheless, after two days of photoconversion at blue light, the dispersions showed no change. As another approach, we tested nanoparticles with a smaller diameter.

Ag nanoseeds were obtained by using $NaBH_4$ as reducing agent and Na_3Cit as stabilizer, by a method standardized in our research group, these particles have an average diameter of 7 nm and so can be called nanoseeds. As mentioned before, the use of $NaBH_4$ leads to the synthesis of particles with a small size. The dispersion was tested in the photoreactor with blue light for two days, after which the system showed an orange-pink color as well as a green color when a dark background is used. This change indicates that the most important factor that must be controlled to start a photoreaction, in this case, is the seed size. Therefore, we used Ag nanoseeds obtained with $NaBH_4$ and Na_3Cit as reducing and stabilizing agents for the photoconversion studies.

Tests for the Ag nanoseeds photoconversion were carried out for at least 5 days to ensure complete photoconversion, the lights used were red, green, blue, white, orange, and aqua; it must be mentioned that red, green, and blue lights were produced by one LED chip each one, whereas orange and aqua were obtained by the combination of two colors: red and green in the case of orange, and green and blue in the case of aqua; also, the white color was obtained by the three main chips simultaneously: red, green, and blue. Fig. 16 shows a photograph of the dispersions obtained after each photoconversion. As it can be observed, the yellow system changed to colors close to blue and purple, and their variations, except for the orange dispersion obtained by blue light; also, Table 2 indicates the excitation light used for the photoconversion, the time required, and the final color of the obtained dispersion.

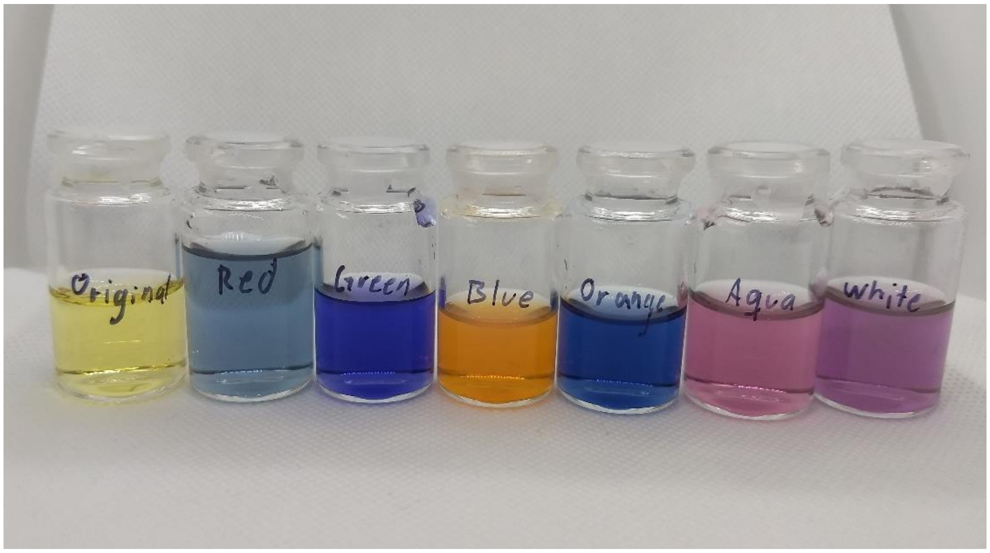

Fig. 16 Photograph of the Ag nanodispersions obtained after their photoconversion at different lights.

Table 2. Photoconversion parameters used and final dispersion outcome.

Excitation light color	**Final dispersion color**	**Conversion time (days)**
No light	Yellow	0
Red	Gray-blue	6
Green	Blue-purple	2
Blue	Orange-pink	1
White	Purple	5
Orange	Royal blue	2
Aqua	Purple	2

On the other hand, Fig. 17 shows the UV-Vis spectra of the dispersions obtained by photoconversion. It can be observed that the spectra are similar except for the one obtained by using blue light, and they resemble the characteristic UV-Vis spectrum of Ag triangular nanoprisms [47]. It is known that the optical properties of AgNT dispersions depend on the nanoparticle size, showing an absorption band that can be shifted between 500 and

900 nm as their edges grow longer [63-65]. The UV-Vis results are similar to the behavior of AgNT dispersions with different sizes, depending on the irradiation wavelength used; nevertheless, the photoconversion outcome could also be a nanodispersion with a different shape or even a mixture of two or more forms. On the other hand, the system resulted from blue light irradiation showed a different behavior as it can be observed in the UV-Vis spectrum. This dispersion shows four absorption bands between 300 and 500 nm, different from the bands expected by AgNT. This orange-pink system shows a similar color and spectrum than the ones observed in AgND [66,67]; also, some works reported the photoconversion of Ag seeds to decahedra using blue LEDs [68].

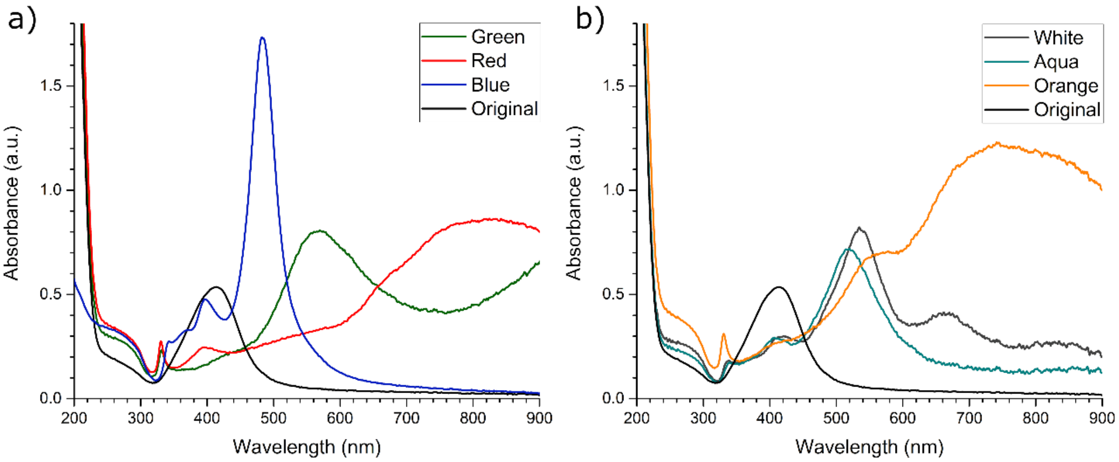

Fig. 17 UV-Vis spectra of the dispersions obtained by photoconversion with different lights: a) green, red, and blue light, and b) white, aqua, and orange light.

To understand the photoconversion mechanism and the minimum conversion time required, kinetical studies were performed using blue and orange lights, producing the AgND- and blue AgNT-like dispersions, respectively. Fig. 18 shows the kinetical study of the blue light photoconversion, and it shows that after 2 h under the stated conditions, the 400 nm absorption band decreases, and a second band appears close to 490 nm. After

24 h, the 490 band shows a high absorbance while the 400 nm band is less prominent, and several bands can be observed at the 340 – 420 nm range. Also, it can be observed that even after 50 h, the UV-Vis spectrum showed no change, indicating a photoconversion time of 24 h.

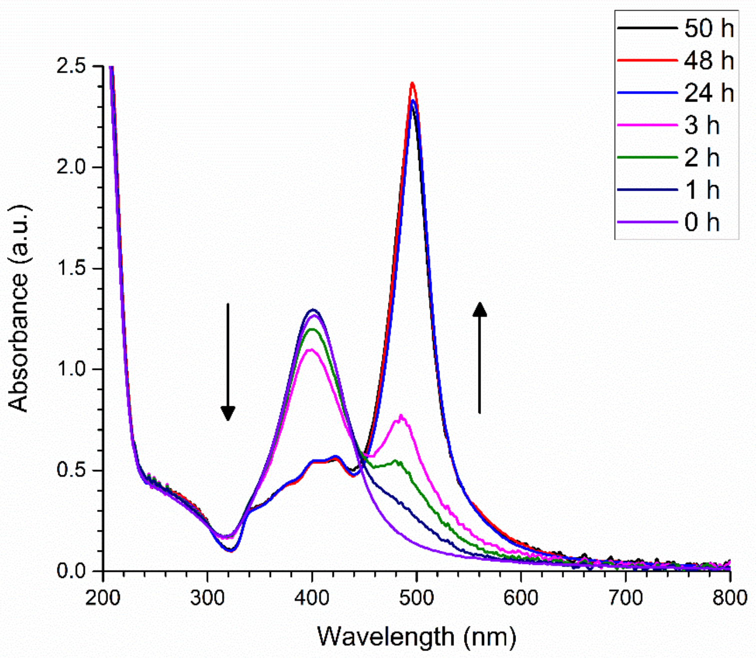

Fig. 18 Kinetical study of the Ag nanoseeds photoconversion under blue LED light.

On the other hand, Fig. 19 shows the kinetical study of the photoconversion when orange light is used. The spectra show that after 12 h, the 400 nm absorption band decreases while two more grow close to 560 and 730 nm, and this behavior continues for up to 144 h, nevertheless, the change between 72 h and 144 h of photoreaction is minimal, this led us to set the photoconversion time to 3 days to standardize the procedure.

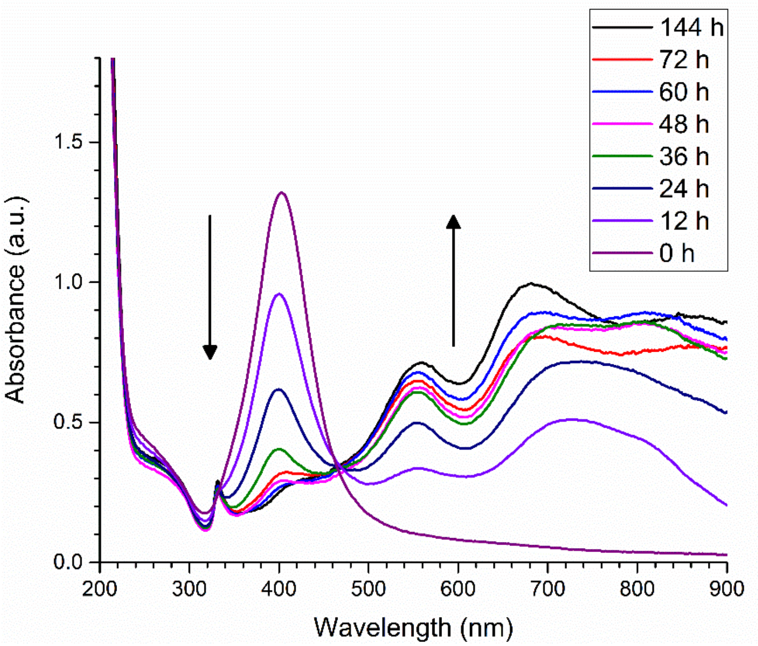

Fig. 19 Kinetical study of the Ag nanoseeds photoconversion under orange LED light.

Even though these results let us know that a morphological change of the Ag nanoseeds occurred, FE-SEM and TEM analyses were carried out to complete the dispersions characterization. First, FE-SEM of the AgND and AgNT were performed, the micrographs are shown in Fig. 20 and Fig. 21, respectively. The AgND micrograph shows the obtainment of small decahedra with an average size of 55.9 ± 3.0 nm, also, it can be observed that even though most of the particles show a decahedral shape, a small percentage of the particles show a spherical-decahedra or triangular pyramidal structure. This can be explained by reviewing the decahedra formation mechanism, in which, according to the literature [69], there are two decahedra formation mechanisms: the first, is known by the growth of small seeds into penta-twinned particles, in which the decahedral planes are subtle yet visible, then, these particles grow through spherical decahedra into small decahedra with its planes fully formed, at this stage the decahedra are easy to recognize among the spherical seeds, and finally, this particles grow into larger decahedra; the second mechanism involves the formation of pyramidal particles that grow larger and assemble to form a large decahedra. The first mechanism explains the presence of spherical decahedra in the micrograph, which indicate that these particles were still growing into decahedra. On the other hand, the second mechanism explains the formation of pyramidal structures in the dispersions, that even though most of the particles are fully grown decahedra, the presence of just a few pyramidal particles and the number of small particles indicate that the formation of penta-twinned seeds is favored in this system.

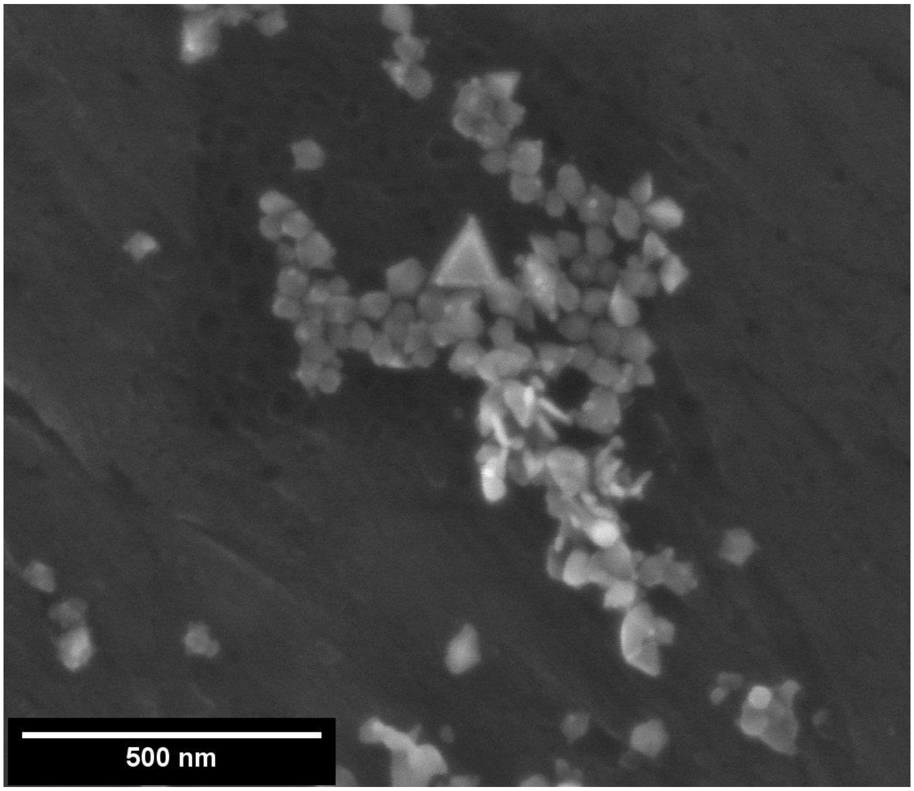

Fig. 20 FE-SEM micrograph of the AgND dispersion obtained using blue light.

By analyzing the micrograph of the AgNT dispersion obtained using orange light (Fig. 21), it can be noted that triangular nanoprisms were obtained with an average edge size of 130.1 ± 10.2 nm and an average thickness of 17.2 ± 1.6 nm, which confirms the predictions made with the UV-Vis spectra. However, along with the larger prisms, smaller (77.5 ± 7.8

nm) prisms and rounded prisms can also be observed. It is important to remark that as the photoconversion procedure involves the formation of light colors with three main color LED chips, the nanoparticles obtained in this dispersion are the outcome of two photoconversions occurring simultaneously, in this case, the red and the green photoconversions, explaining the wide range of sizes obtained by using orange light. Also, this can be confirmed by analyzing the UV-Vis spectra (Fig. 17) shown by the dispersions obtained using red, green, and orange lights: the absorption bands obtained by the orange dispersion are the outcome of the dispersions obtained by green and red light together. Therefore, searching for a monodisperse system, the rest of the experiments were carried out using the dispersion obtained with green light, from now on, referred to as AgNT.

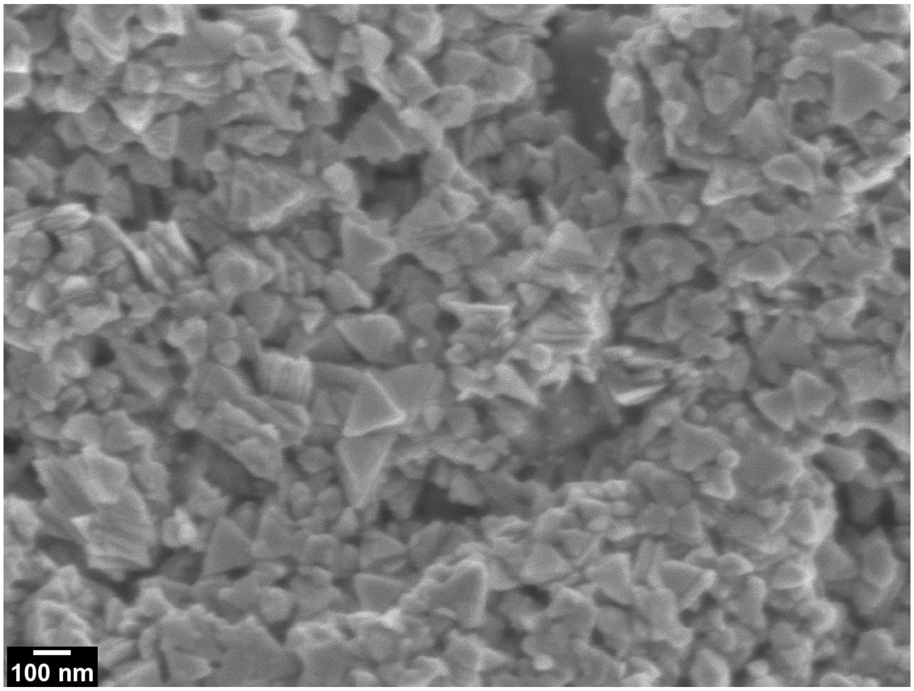

Fig. 21 FE-SEM micrograph of the AgNT dispersion obtained using orange light.

To analyze the morphological properties of the new AgNT dispersion, TEM analysis was carried out, here presented in Fig. 22. In this micrograph, triangular nanoplates can be observed with an average edge size of 92.6 ± 7.7 nm, as well as a few additional structures as small spheres and short rods, nevertheless, this dispersion has a higher monodispersity than the one obtained by irradiating orange light and therefore it was chosen as our new AgNT dispersion. It must be remarked that the prisms show rounded corners, which is an important factor for the hot-spot formation in a SERS substrate.

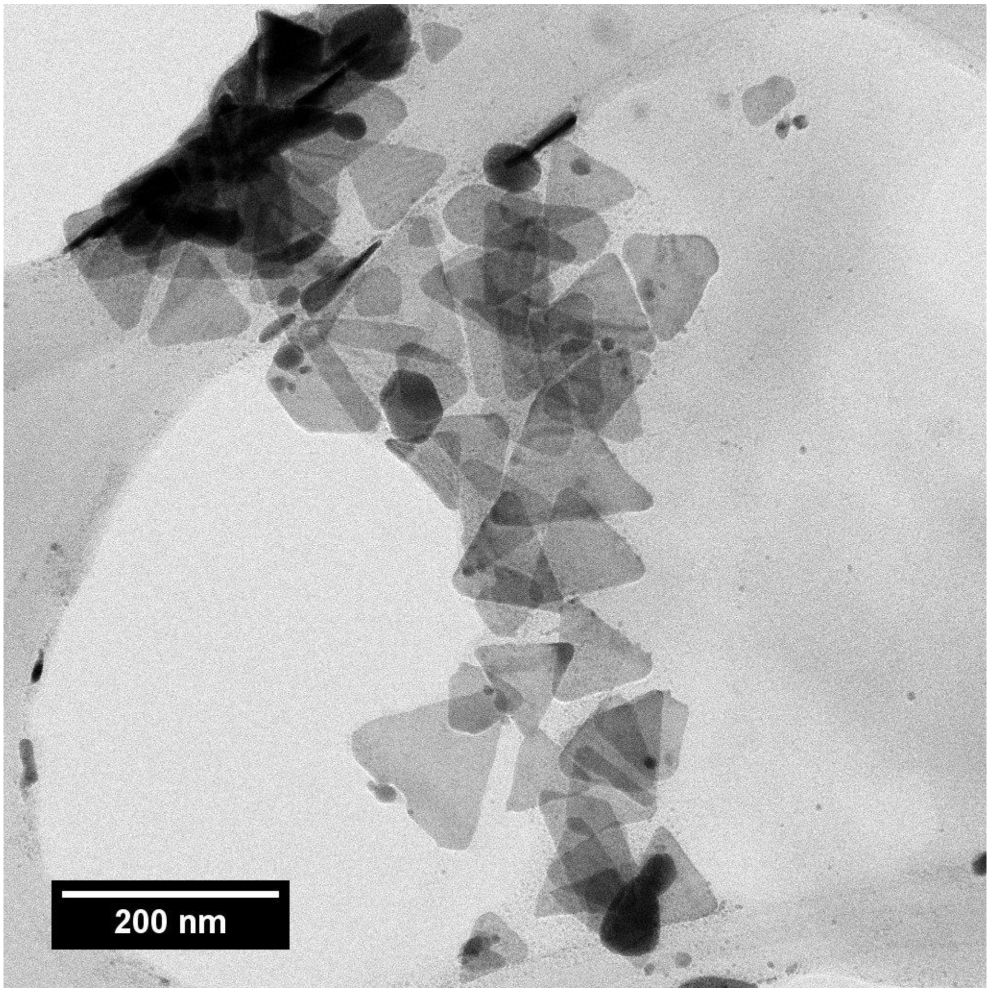

Fig. 22 TEM micrograph of the AgNT dispersion obtained using green light.

4.2 SERS microfluidic chips fabrication

4.2.1 Fabrication and analysis of SERS substrates

Before the implementation of the SERS microfluidic chips, studies of the fabrication of regular SERS substrates must be carried out. To study the performance of the obtained Ag nanostructures dispersions as SERS devices, substrates were fabricated by a simple method. In this procedure, the nanoparticles must be first concentrated by centrifugation at a suitable speed until a nanoink is formed; this system is then deposited onto previously (mechanically) polished Al substrates. For the latter, two deposition conditions were studied to reduce the coffee ring effect.

The coffee ring effect refers to a phenomenon that occurs when the solvent evaporation rate is fast, leading to areas with a higher concentration of the dissolved/dispersed species, as it can be observed when the last amount of coffee evaporates at the bottom of our favorite mug. At the laboratory, this effect is very common when a drop-casting technique is used, avoiding the obtainment of uniform deposits or layers of our objective species. In the case of this work, the reduction of the coffee ring effect allows us to fabricate uniform SERS substrates, thus increasing the analysis reproducibility. Therefore, we performed a quick analysis by fabricating SERS substrates at higher humidity conditions. As the coffee ring effect is reduced when the evaporation rate is slower, by increasing the humidity conditions inside a deposition chamber, the resulting nanoparticle coating will show a higher uniformity when the humidity is higher.

For these experiments, the polished Al substrate is first set onto a glass slide contained inside a water-filled Petri dish, then, the Ag nanoink is drop-casted onto the substrate and the dish is closed. After 24 h, the nanoink droplet was flattened and the substrate can be taken out to standard environmental conditions to allow the solvent to evaporate. These conditions led to uniform SERS substrates when the active material consists of AgNT and AgND, however, it was noticed that for AgNS, uniform substrates can be obtained by simple drop-casting at room humidity conditions. Fig. 23 shows a photograph of SERS substrates obtained using different dispersions, being able to appreciate the homogeneous active area of each substrate.

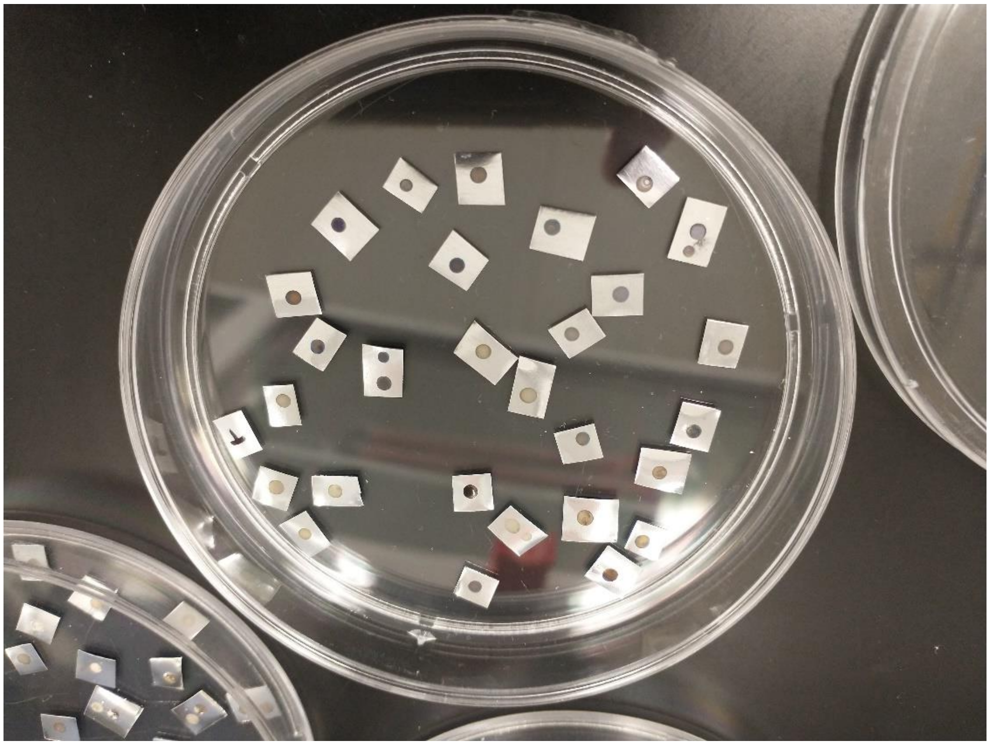

Fig. 23 Photographs of SERS substrates fabricated onto polished Al.

As a first SERS study for this work, the fabricated substrates were used to analyze *p*-ATP, as it is a model molecule and its commonly used prior to any specialized detection. This first study reveals the real performance of each dispersion when used as a regular SERS substrate, which also allow us to understand the impact of the nanostructure shape on the general SERS effect. It must be mentioned that the Raman probe was deposited by drop-casting 3 μL of the suitable solution onto the substrates and let dry prior to its analysis. Also, the instrumentation parameters used were: a 780 nm laser at 2.2 mW and 10 s as integration time for the AgNS and AgNT, and 1 s for the AgND substrates, using a Thermo Scientific DXR Raman microscope with a 50X objective lens. The SERS spectra obtained for each type of nanostructure are shown in Fig. 24, 25 and 26 for AgNS, AgND, and AgNT, respectively.

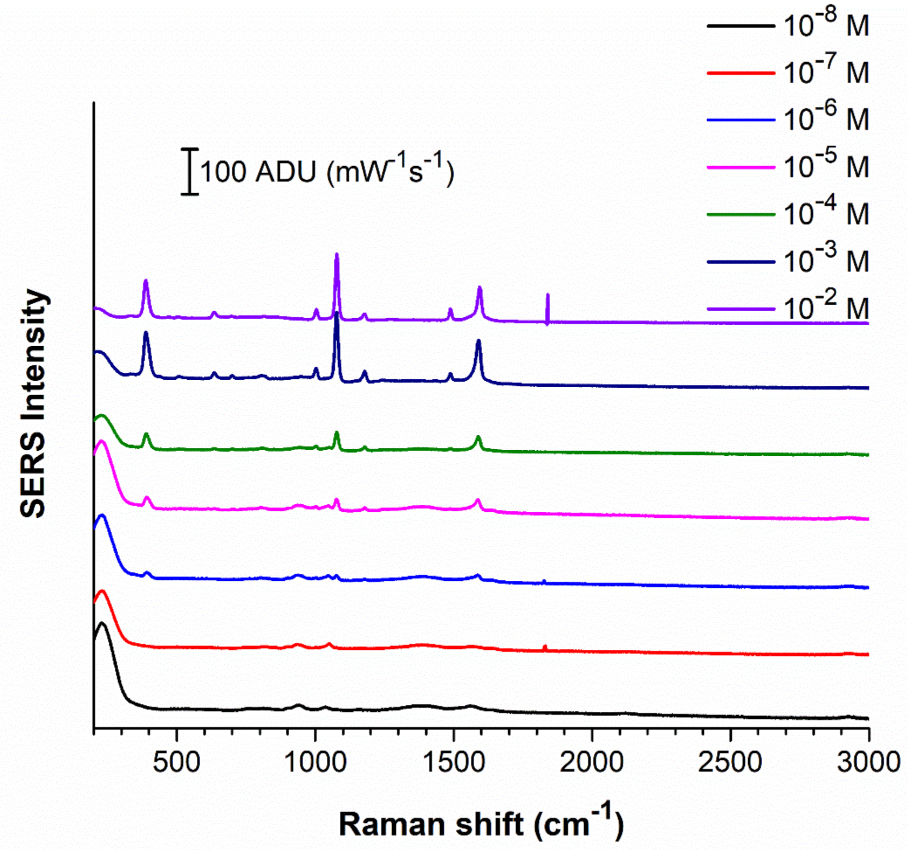

Fig. 24 SERS spectra of *p*-ATP at a concentration range of 10^{-2} to 10^{-8} M analyzed using AgNS-based substrates.

An additional note is that, in this work, the concept LOD is used; nevertheless, the LOD reported in SERS is not calculated by analytical calculations, in the state-of-art it is common to use this concept as a synonym for the minimum concentration detected by the instrument, that is to say, the minimum concentration at which the characteristic bands of the analyte can be distinguished from any noise or substrate / background bands.

Fig. 24 shows the Raman spectra obtained using substrates based on AgNS. It can be observed that the characteristic vibrational bands of *p*-ATP can be observed at concentrations higher than 10^{-5} M, increasing its intensity as the concentration becomes higher. At lower concentrations, the Raman peaks observed correspond to the substrate itself, and they should not be confused with any probe, as those are bands of molecules close to the particles, such as the stabilizing agent itself.

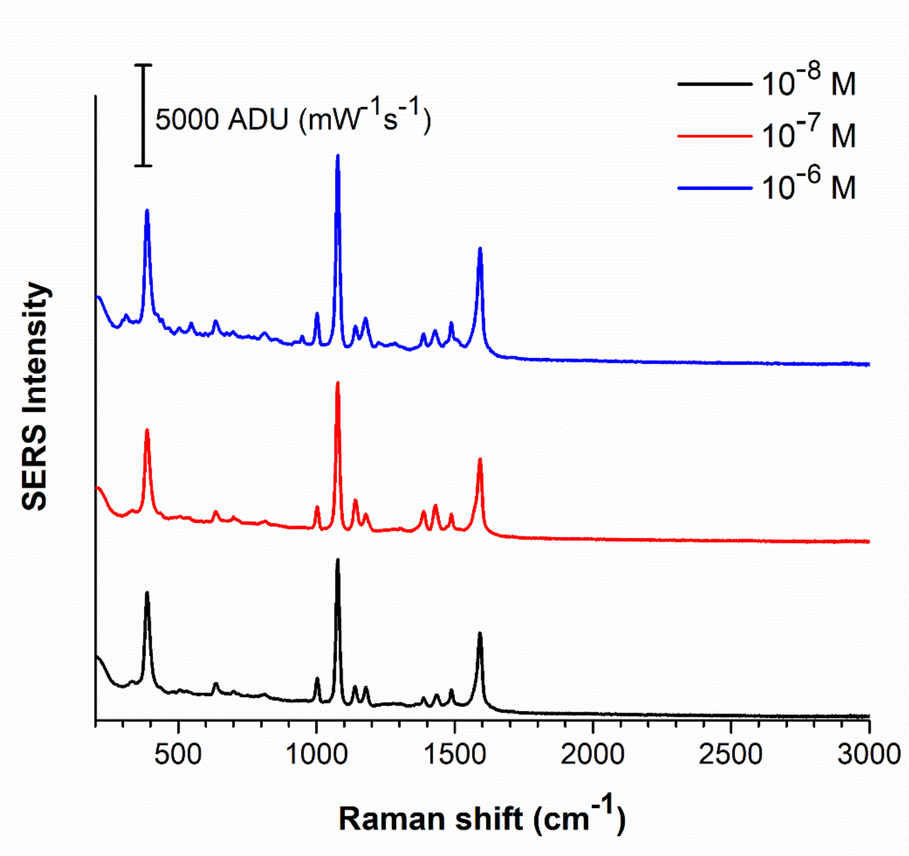

Fig. 25 SERS spectra of *p*-ATP at a concentration range of 10^{-6} to 10^{-8} M analyzed using AgND-based substrates.

On the other hand, the spectra obtained by analyzing *p*-ATP with AgND-based substrates are shown in Fig 25. The difference between AgNS and AgND substrates can be immediately observed, as decahedra led to Raman intensities high enough to saturate the equipment detector, therefore the integration time had to be changed from 10 to 1 s. The high sensitivity shown by this kind of substrates allowed the detection of *p*-ATP at 10^{-8} M with intense vibrational bands, showing that the real LOD is below this concentration. Yet, the results indicate the potential of using this shape to fabricate SERS substrates sensitive enough to analyze samples at a lower concentration than those detectable by using isotropic nanoparticles.

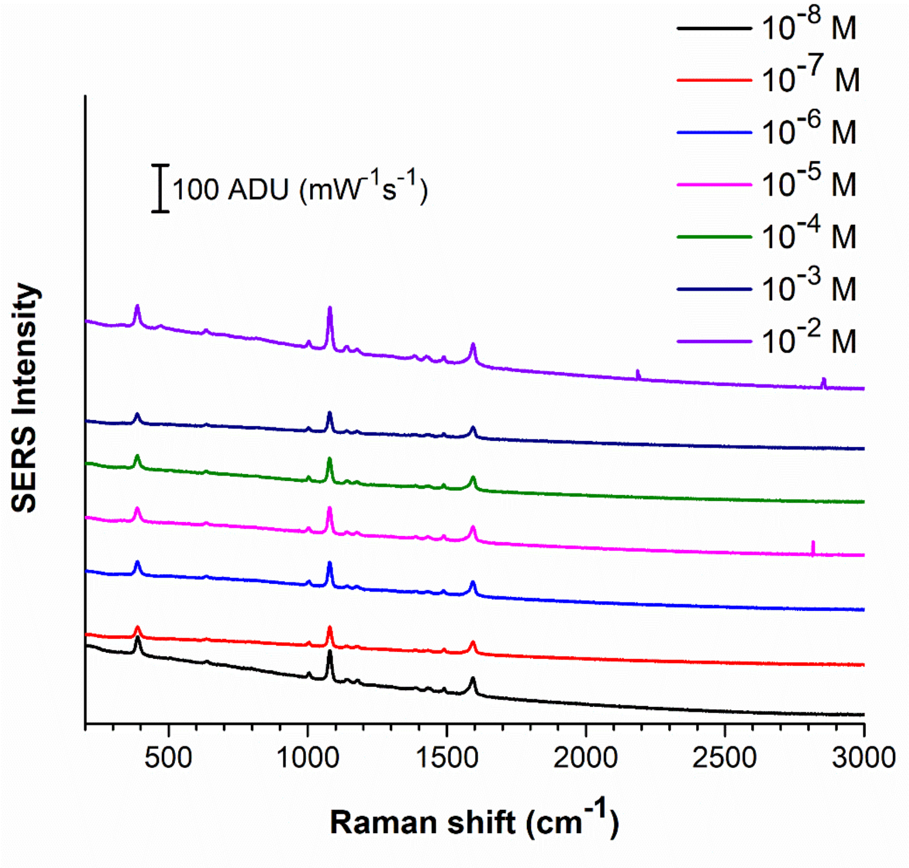

Fig. 26 SERS spectra of *p*-ATP at a concentration range of 10^{-2} to 10^{-8} M analyzed using AgNT-based substrates.

Lastly, Fig. 26 shows the LOD study performed using AgNT as active SERS material. It must be mentioned that, as the SERS analyses were performed prior to the TEM studies, the particles used for these substrates were those obtained using orange light, that is, a dispersion containing large and medium nanoplates with rounded edges. The spectra show that this kind of substrates allow us to detect the Raman probe at concentrations as low as 10^{-8} M as well; however, the intensity of the bands is not as high as those obtained using AgND, which indicate that even though using nanoplates lead to higher electromagnetic field enhancements, these are not as high as those obtained using decahedral particles. Also, it can be observed that the intensity reached does not increase significantly as the concentration rises, this is often a sign of substrate saturation, which occurs when the analyte molecules form a layer that interacts directly with the nanoparticles, however, this layer act as a barrier that avoids the interaction between additional molecules and the active material. This is often observed as a “fixed” intensity that is independent of the molecule concentration, as long as it is higher than the concentration required to form the barrier layer.

It can be highlighted that those substrates fabricated with AgND as active material showed the highest sensitivity, with a LOD lower than 10^{-8} M of *p*-ATP. This can be easily explained as this shape has more edges and peaks than those observed in the AgNS and AgNT dispersions, allowing the formation of a larger number of hot-spots in the substrate, also, this shape might lead to a 3D arrange of hot-spots, which is not easily reached with other shapes such as nanoplates. This remarks the importance of choosing the right morphology or active material for SERS substrates, depending on the instrumental parameters available (laser, laser power, integration time, focus distance), the chemical matrix of the sample, the Raman probe affinity, and the sensitivity required.

4.2.2 Fabrication of 3D and shrunken microfluidic chips

As mentioned, our approach for the fabrication of microfluidic chips is by first 3D printing the chips and then using shrinkable PU to obtain a positive mold, which will be used to obtain a PDMS substrate that contains the microfluidic channels. As a first approach, two microfluidic chip designs were printed: a Y-junction chip, and a second chip that contains a single inlet and outlet configuration as well as a mixing path. Both chips were printed in PLA with a 0.6 mm nozzle and 0.2 mm profile, this refers to the precision of the instrument, the smaller the profile, the higher precision and detail can be obtained. Along with the chips, a "universal test mold" was printed; this object contains different shapes that allow the testing of the PU shrinking properties. A photograph of the 3D printed objects can be observed in Fig. 27.

As observed, the printed objects show a clean surface, with no extra or missing parts. As a second step, PU shrinking tests were carried out using the universal test mold, adding a mixture of water and PU at a 4:1 volume ratio. The liquid PU is colorless and shows a high viscosity; however, when it interacts with water, the system becomes white, and it solidifies after 40 – 60 s. The positive PU mold was then detached from the printed mold and let dry under atmospheric conditions for 4 days, however this process can also be carried out in a drying oven at 50 °C for 48 h. As the water molecules evaporate from the solid system, the PU chains get compressed and thus the object gets smaller in size. This process occurs in the 3 axes, leading to a uniform shrinkage.

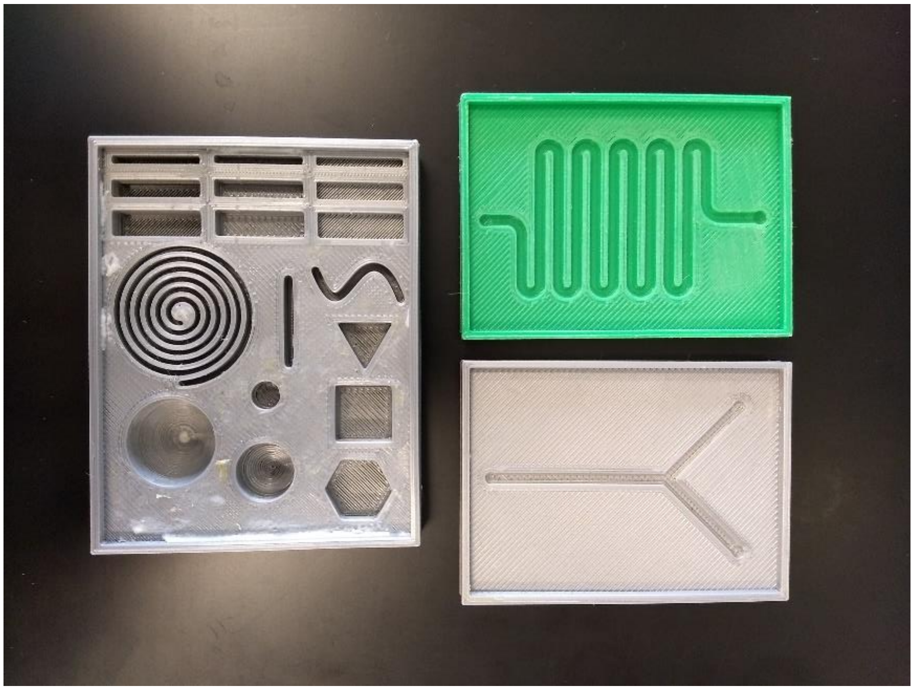

Fig. 27 Photograph of the 3D printed microfluidic chips and the universal test mold.

In Fig. 28, a photograph of the three stages of the shrinking process can be observed: first, the 3D printed mold is shown; then, a white PU positive mold is obtained after pouring the polymer, this mold preserves the features of each one of the shapes included in the master mold; lastly, the yellow mold is a PU mold after the shrinkage process, it shows the same shapes and size ratios as the pre-shrinkage mold. It must be mentioned that the yellow mold show bubbles; nevertheless, these bubbles are inside of the mold and do not affect the surface of the mold itself.

As a second test, shrinkage tests were carried out using the Y junction chip. As it can be observed in Fig. 29, the shrunken mold shows the same size ratios as the original chip, as a 3.5 cm x 4.9 cm object with microfluidic channels with a thickness of 1.8 mm, showing that the 3D printing and PU shrinkage methods are suitable for the fabrication of small devices with high structural precision at a low cost. The shrinkage percentage of the PU mold is 59.5 ± 3.4% in each axis in this case.

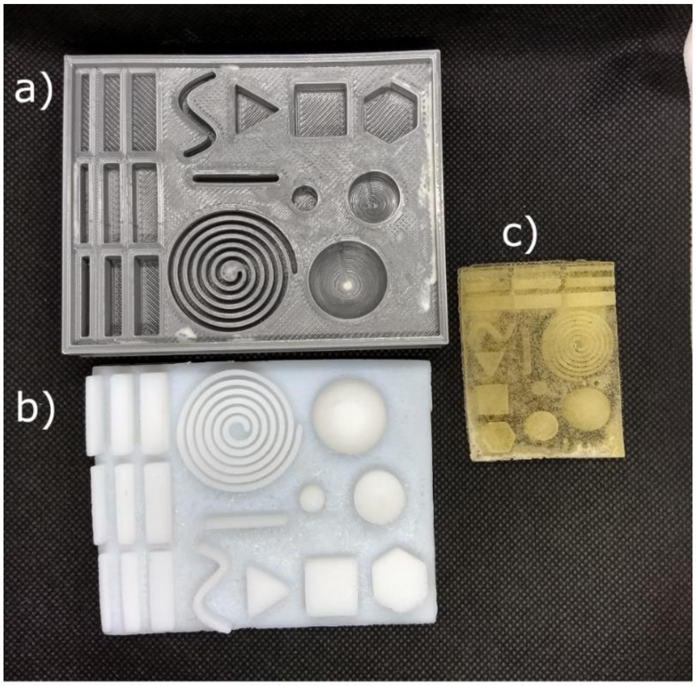

Fig. 28 a) 3D printed universal test mold, b) PU positive mold before the shrinkage process, and c) shrunken PU positive mold.

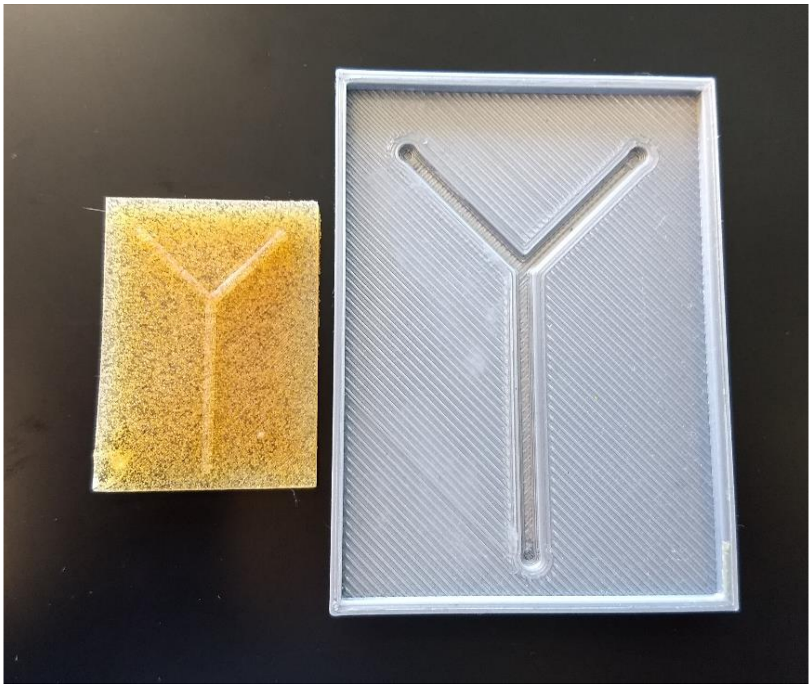

Fig. 29 Photograph of the 3D printed Y junction chip and its shrunken PU positive mold.

By printing chip molds at a smaller size, PU shrunken molds with 800 μm channels can be easily obtained, however, this is limited by the 3D printer precision (nozzle size, infill, chip design, and used profile) when using an extrusion printing technique. It is important to mention that, when working with fluids at a micrometric channel, it is common to have problems with the mixing of a system, as both flows reach a laminar regime, and they flow parallel from each other. To overcome this problem, some chips are designed with obstacles that act as micro-mixer structures, allowing the diffusion of each flow into each other. Another strategy is to design a channel long enough to let the flows diffuse themselves into the other, however, mixing structures are still required to ensure a proper mix. This behavior must be considered while designing microfluidic chips, especially if the objective is to flow two solutions or dispersions that must be mixed for their final use, such as in SERS analyses, where nanostructures must be in contact with the Raman probe. Considering this information, another chip was printed and shrunken with PU, this one show mixing structures along the channel, as shown in Fig. 30.

As the next step, the final PDMS chips were obtained using the shrunken molds. At first, the chips contained bubbles embedded, which was solved by setting the pre-cured PDMS into vacuum conditions for several minutes to pull all trapped air to the surface. To build the final device, the microchannels-containing chip and the second material (usually glass or a flat PDMS substrate) must be cleaned to remove any debris or unwanted material, then they undergo plasma treatment to eliminate any residual organic compound; also, this treatment changes the surficial chemistry of both substrates, allowing them to form a permanent bond, thus sealing the chip itself to avoid any flow leaking. This device is then heat treated at 70 °C for 2.5 h to remove residual moisture and ensure a proper bonding between both materials.

Fig. 30 3D printed chip containing mixing structures along the main channel, and its PU shrunken mold.

The final microfluidic chips are now ready to be decorated with nanostructures to be used as SERS substrates, as shown in Fig. 31. This can be done by different procedures, such as functionalizing the microchannels with a nanostructure-compatible material, drop-casting the dispersions in the channels, or even by *in-situ* preparation of the nanoparticles. In our case, we performed a decoration method similar to the standard SERS substrates method: drop-casting. For this, the microchannels were flooded with nanoparticle paste, then the tubbing was removed, and the chip was left to dry at high humidity conditions. Once the chip was dry, the color of the microchannels changed to gray, indicating the deposition nanoparticles along the channels.

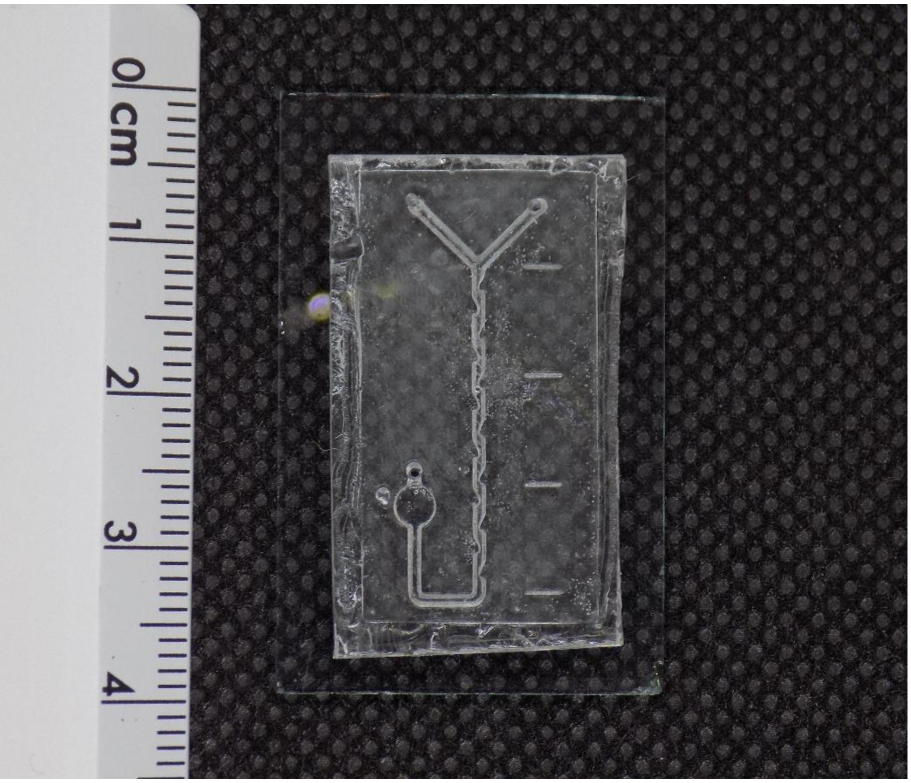

Fig. 31 PDMS-glass microfluidic chip prepared using the PU positive mold.

The chip was observed using an optical microscope after the flooding procedure, as shown in Fig. 32, which shows the analysis area of the microchip, and it can be observed that the channels are decorated with nanoparticle agglomerates in a non-uniform manner. This has a direct effect on the SERS effect potential of the substrate, as the presence of cracks and holes on the exposed surface will lead to different enhancements throughout the microfluidic chip.

Quick tests were conducted to determine if the agglomerates are stable. For this, water and air were flown at different flow rates, including the purge option of the vacuum syringe pump, and no changes were observed throughout the microfluidic channel, indicating a high stability at these conditions.

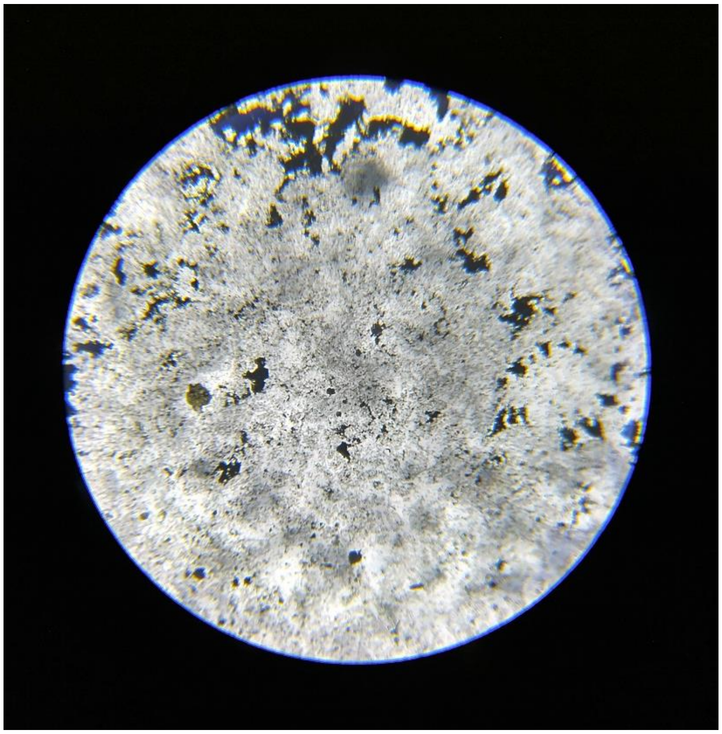

Fig. 32 Photograph of the analysis area in a PDMS-glass microfluidic chip decorated with AgNS via channel flooding deposition.

4.2.3 Fabrication of acrylic microfluidic chips

In a parallel way, acrylic microfluidic chips were also prepared by using a CNC micromilling process. This fabrication procedure represents another cost-effective method for the obtainment of microfluidic chips, as it does not require the complex processes and facilities often required for lithography. In this case, the microchannels size depends only on the drill bits used and the chip design itself. The first step is to set a 1.3 mm thick acrylic sheet on the CNC work area, define the origin, and operate the machine to drill the desired design. It must be mentioned that the microchannels themselves were obtained using a 200 nm drill bit, whereas the inlets and outlets required an 800 nm bit and a second acrylic sheet. Both sheets undergo a cleaning process to eliminate debris, and then they are bonded by a two steps procedure: first exposing both substrates to a $CHCl_3$ vapor ambient, and then pressing them together while applying heat. Lastly, tubbing was glued to the inlets and outlets of the chips, being careful enough to seal the chips without clogging the microchannels. Fig. 33 shows an acrylic chip after its fabrication as well as with tubbing and syringes plugged.

These acrylic chips showed a quicker alternative for the obtainment of precise microfluidic chips with narrower channels than those obtained by our 3D-shrinking process. However, the use of acrylic instead of glass or PDMS implies a probability of additional Raman bands that can interfere with the Raman probe signals, therefore exploratory experiments must be carried out to ensure the selection of a suitable probe.

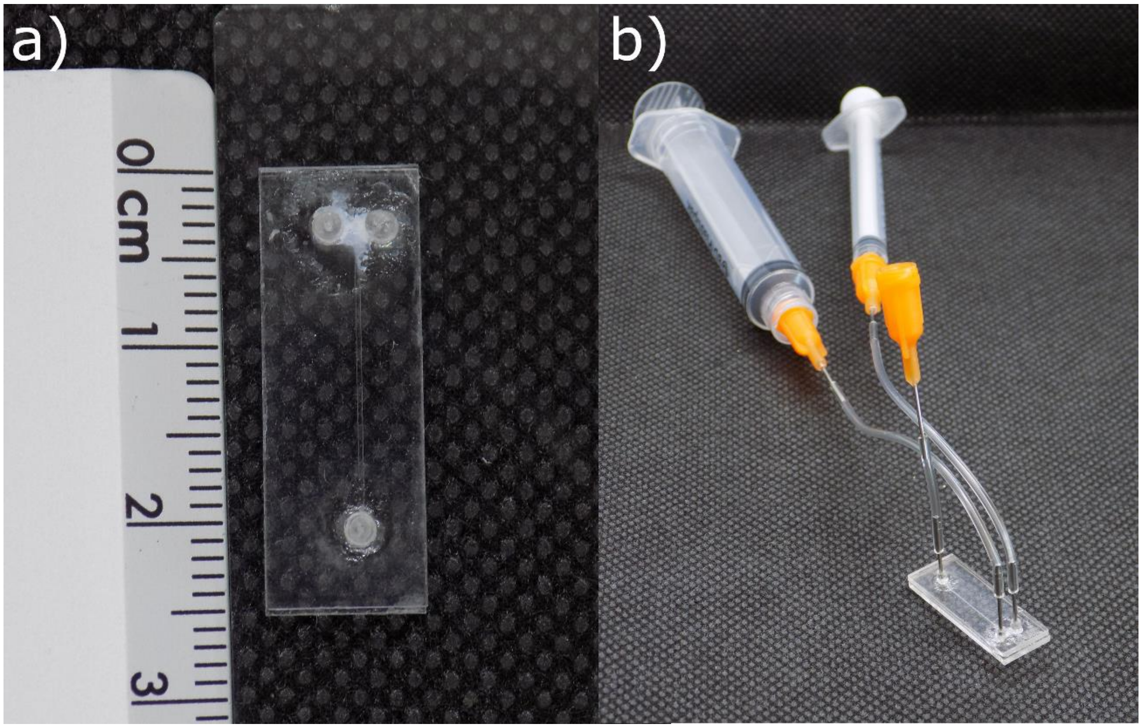

Fig. 33 a) Aerial view of an acrylic microfluidic chip, and b) acrylic chip with tubbing and syringes set.

As a next step for the SERS microfluidic chips preparation, the acrylic chips were exposed to different procedures to decorate the inner walls, including activation by solvents, functionalization, and direct casting. In the solvent activation process, a solvent that attacks the acrylic is flown to activate the microchannels and allow the deposition of nanostructures. Acetone and toluene were tested for a few seconds, however, the inner walls collapsed, clogging the chip itself.

As a second process, the microfluidic channels underwent functionalization using MPTMS to provide SH- moieties that can easily interact with noble metal nanostructures and leading to a self-assembled nanostructure coating. This process was carried out as follows: first, toluene was flown for 2 min, followed by 1mM MPTMS in toluene for 30 min as toluene slowly dissolves acrylic, then toluene for 2 min, any solvent residue was washed with water for 5 min, then air was flown for 5 min, followed by a nanostructure dispersion flown for 4 h, washed with water for 30 min, and dried with air for 5 min, all of the steps were performed at a flow of 1 mL/h. However, the microchannels showed no change, thus meaning that MPTMS did not interact with the inner walls, avoiding the deposition of nanoparticles in the chip. These results indicate that another functionalizing agent is needed, specifically a molecule with a high affinity with the chemical structure of both, the nanostructures, and the acrylic sheet.

As the next approach, we decided to perform the flooding deposition method early described. The microchannels changed its color, indicating the deposition of nanostructures along the 200 μm channels. The chips were observed in an optical microscope prior and after this procedure, as shown in Fig. 34. The first photograph shows the microchannels before the particle flooding, and it can be observed that the path is overall clean and free from any material except for some residual debris; however, after the nanoparticle flooding, the photograph shows material deposited at the bottom of the channels, in this case, AgNT agglomerates were deposited uniformly throughout the microchip channels, from the outlet to the inlets, showing a potential decoration for SERS studies.

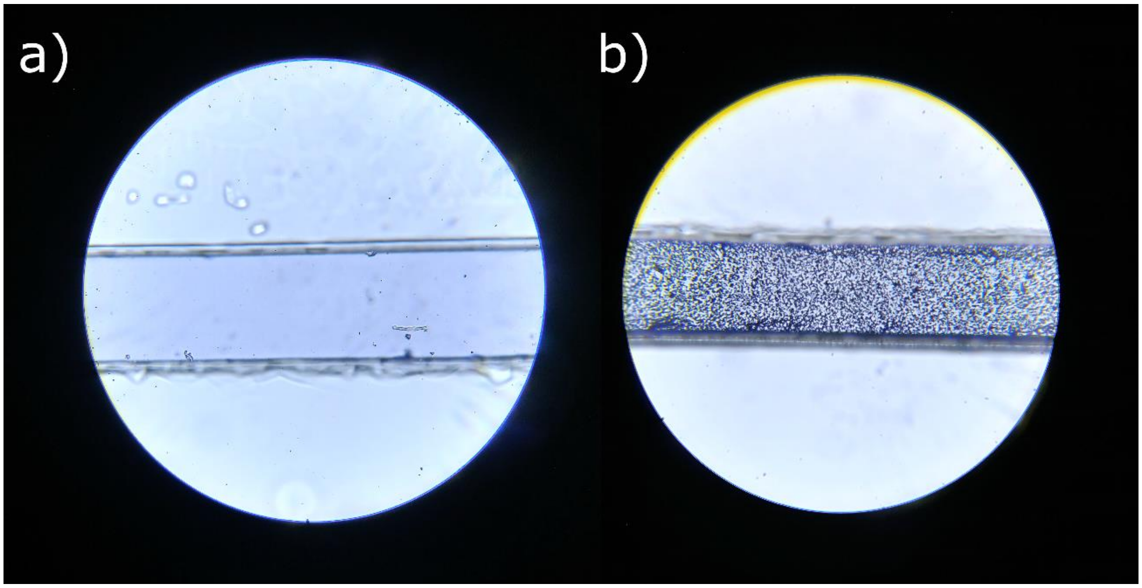

Fig. 34 Photographs of a microchannel a) before, and b) after flooding deposition with AgNT paste.

Similarly to the PDMS-glass chips, the decorated acrylic microfluidic chips, underwent tests to determine if the agglomerates coating is stable. For this, water and air were flown at different flow rates, and no changes were observed throughout the microfluidic channel, indicating a high stability at these conditions, and thus, the chips are now ready for SERS studies.

4.2.4 SERS performance studies

Fig. 35 shows photographs of some PDMS-glass and acrylic SERS microfluidic chips ready for their use, where their size differences are easily remarked.

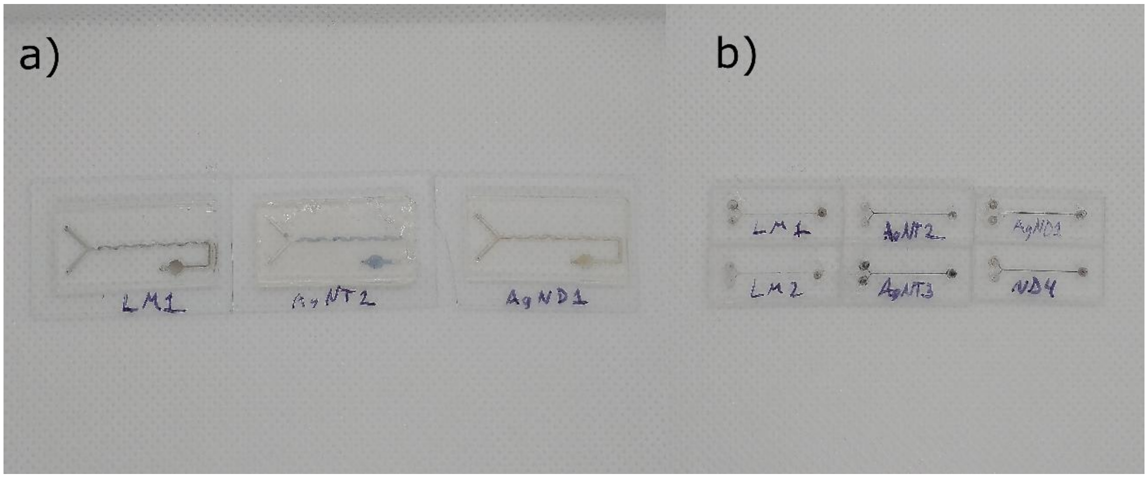

Fig. 35 Photographs of a) PDMS-glass, and b) acrylic SERS microfluidic substrates.

The first kind of chips tested were the PDMS-glass substrates, for this, 10^{-3} M *p*-ATP was used as analyte. The SERS spectra obtained are shown in Fig. 36, which allow us to observe that the three morphologies are suitable for their use as SERS substrates; however, the enhancement of the vibrational bands differ from the results obtained by the normal SERS studies. In this case, the lowest enhancement was reached by AgND-based chips, which can be a result of the non-uniform coating of particles along the microchannel, as the flooding procedure was particularly harder to control in the PDMS-glass substrates, leading to areas with different concentration of nanoparticle agglomerates. This behavior also impacts the reproducibility of the substrates.

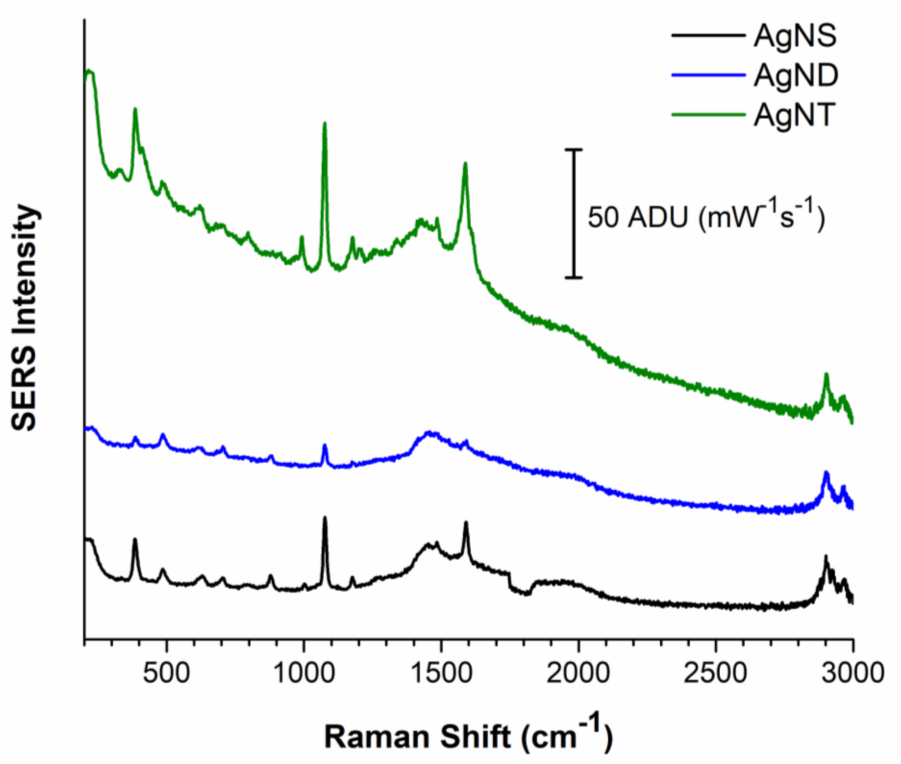

Fig. 36 Raman spectra of 10^{-3} M *p*-ATP analyzed using PDMS-glass SERS microfluidic chips.

On the other hand, the SERS spectra obtained by the analysis of 10^{-3} M *p*-ATP using the acrylic SERS microfluidic chips can be observed in Fig. 37. In this case, significant increases in Raman intensities are shown, with AgND-based chips as the ones with the highest enhancement. In contrast with the PDMS-glass substrates, the fabrication procedure for the acrylic chips lead to products with no leakage, which allow a slower solvent evaporation rate and thus the nanoparticle aggregates are uniformly deposited. Also, as the PDMS-glass substrates are produced using a 3D printed mold, the final channels are not completely circular, they show the layer-by-layer morphology observed in extrusion-printed objects. This morphology changes the flow of any liquid and act as long traps for big species such as nanoparticles agglomerates.

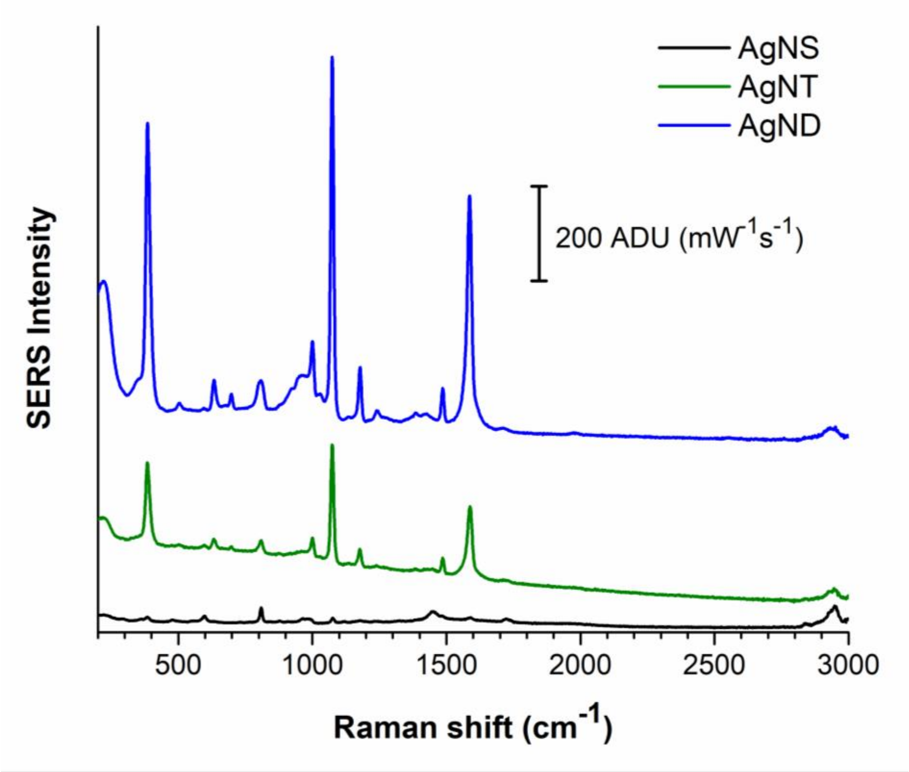

Fig. 37 Raman spectra of 10^{-3} M *p*-ATP analyzed using acrylic SERS microfluidic chips.

Even though both kinds of SERS chips were obtained by low-cost procedures that can be further optimized, the substrates made with acrylics showed the best results and thus, these were selected to perform the reproducibility and LOD studies, specifically the AgND-based acrylic substrates, which showed the highest intensity enhancement.

In recent years, reporting the reproducibility of the SERS substrates has become a task that validates and strengthens the results of any new research. This parameter is vital to compare most of the SERS substrates found in the state-of-the-art and it can be used as a deciding factor when a researcher or laboratory is looking to add SERS analysis to their repertoire.

In this study, the reproducibility test was carried out by collecting Raman spectra (using 10^{-3} M *p*-ATP as analyte) all along the microfluidic channels, allowing us to calculate the relative standard deviation (RSD) of the analysis. In the case of a real sample analysis, the RSD of a SERS substrate refers to the capability of the substrate to collect spectra with similar intensities regardless of the area analyzed within the substrate. For the SERS microfluidic chips fabricated using AgND nanoparticles as active material, an RSD value of 26.67% was obtained, and this value can be graphically observed by the Raman intensities shown in Fig. 38.

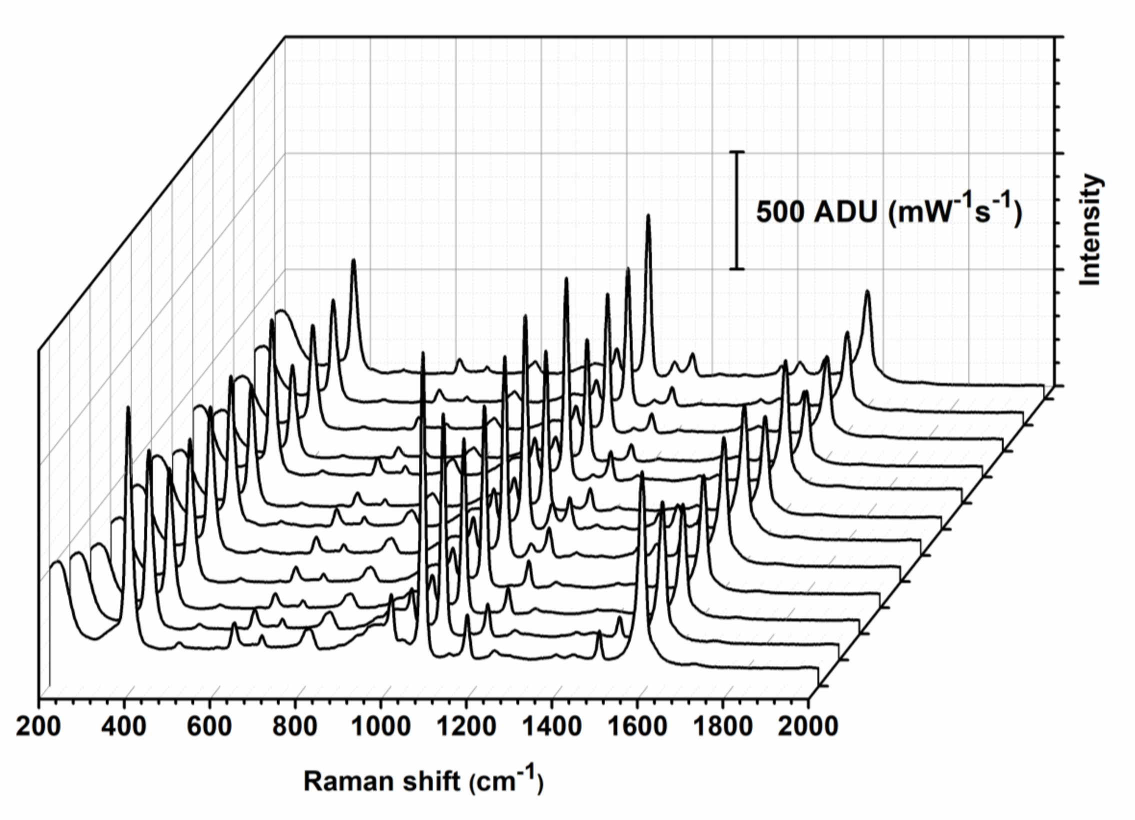

Fig. 38 SERS spectra of 10^{-3} M *p*-ATP analyzed at different spots of an acrylic AgND microfluidic chip.

It shall be mentioned that, to lower the RSD value of the substrates fabricated in this project, a better control of the flooding process must be achieved, this will ensure a higher uniformity of the agglomerates coating, leading to a decrease in the SERS effect variation along the microchannels.

On the other hand, to determine the LOD of the AgND-based SERS chips, *p*-ATP solutions at concentrations of 10^{-3}, 10^{-6}, and 10^{-9} M were analyzed, resulting in the spectra shown in Fig. 39.

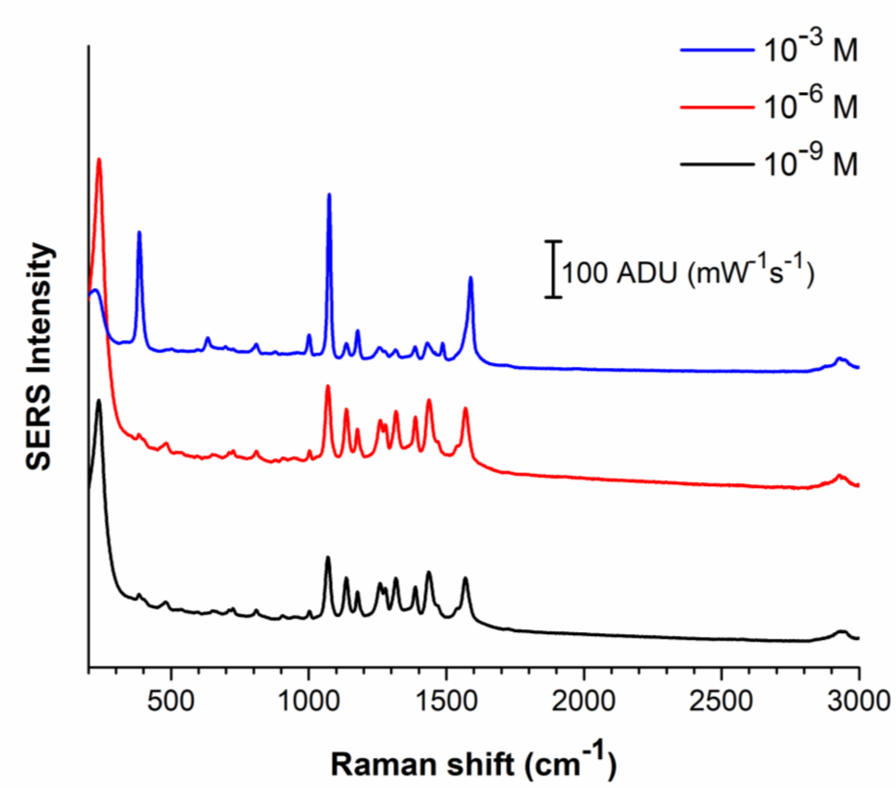

Fig. 39 LOD analysis of the AgND-based SERS microfluidic chips using *p*-ATP at a concentration range of 10^{-3} to 10^{-9} M.

It can be observed that these microfluidic substrates allow the detection of *p*-ATP at 10^{-3} M without any issue; however, at lower concentrations, the spectra contain the Raman signals of *p*-ATP, 4,4’-dimercaptoazobenzene (DMAB), as well as some of the AgND nanoparticle signals. This is due to the high sensitivity of the nanostructure array and the low concentration of the main analyte; in this case, the number of *p*-ATP molecules is not enough to outstand the signals of DMAB, which is a subproduct of the interaction between the analyte molecules and the laser energy, catalyzed by the nanostructured surface provided within the microchannels. This catalyzed reaction is often found in several SERS studies, and it was found to be reversible in a reductive environment [70].

In addition to what has been mentioned, it can be highlighted that the Raman intensities obtained by the 10^{-6} and 10^{-9} M are similar between each other, however the 10^{-3} M analysis shows higher intensities. This indicates the existence of a minimum concentration required to trigger a stronger SERS enhancement, in this case, a concentration lower than 10^{-3} M. These results allow us to reject our main hypothesis, as the AgND-based SERS microfluidic chips did not detect *p*-ATP at 10^{-9} M.

CHAPTER 5

CONCLUSIONS

Based on the results obtained in this work, it can be concluded that:

1. Ag nanospheres (AgNS) were obtained by a citrate-based procedure, according to the optical properties of the dispersion, whose UV-Vis spectrum shows a second absorption band, associated with an LSPR quadrupole mode, thus, indicating the formation of particles with a bigger diameter than those obtained by $NaBH_4$-based methods.

2. AgNS dispersions can not be photoconverted under RGB LED light, even at different pH and free citrate ions concentrations. This is due to the high stability and large diameter of the nanoparticles.

3. Ag nanoseeds obtained by a $NaBH_4$ reduction procedure were able to be photoconverted at red, green, blue, orange, aqua, and white LED light, leading to the obtainment of Ag nanodecahedra (AgND) when using a blue light, and Ag triangular nanoplates (AgNT) with green light. These growth behaviors were followed by kinetical studies through UV-Vis spectroscopy.

4. The nanoparticle dispersions were characterized by FE-SEM and TEM, confirming the obtainment of nanospheres, decahedra and triangular nanoplates with sizes of 38.7 ± 1.9, 55.9 ± 3.0, and 92.6 ± 7.7 nm, respectively.

5. Nanoinks and SERS substrates were successfully fabricated by using the dispersions synthesized in this work, reaching a LOD of 10^{-5}, 10^{-8}, and 10^{-8} M for AgNS, AgND, and AgNT respectively, using *p*-ATP as probe molecule.

6. Microfluidic chip molds were 3D printed and used to obtain shrunken molds made of PU, with a uniform linear shrinking percentage of 59.5 ± 3.4%, which allowed the fabrication of SERS PDMS-glass microfluidic chips by a flooding decoration procedure.

7. Acrylic microfluidic chips were fabricated using a micromilling approach, and their microchannels were decorated with nanoparticles using a flooding procedure, which led to SERS microfluidic chips with their channels uniformly coated with nanostructures agglomerates.

8. PDMS-glass and acrylic microfluidic chips can be used as SERS substrates to detect *p*-ATP; however, the acrylic chips showed a higher potential as reproducible and sensitive substrates.

9. AgND-based acrylic microfluidic chips showed an RSD of 26.67% and a LOD of 10^{-3} M, rejecting the hypothesis of this work.

REFERENCES

1. Cobley, C.M.; Skrabalak, S.E.; Campbell, D.J.; Xia, Y. Shape-controlled synthesis of silver nanoparticles for plasmonic and sensing applications. Plasmonics, 2009, 4 (2), pp. 171-179.

2. Zheng, X.; Peng, Y.; Cui, X.; Zheng, W. Modulation of the shape and localized surface plasmon resonance of silver nanoparticles via halide ion etching and photochemical regrowth. Materials Letters, 2016, 173, pp. 88-90.

3. Liu, Y.; Han, X.; He, L.; Yin, Y. Thermoresponsive assembly of charged gold nanoparticles and their reversible tuning of plasmon coupling. Angewandte Chemie International Edition, 2012, 51 (26), pp. 6373-6377.

4. Wang, Y.; Yang, F.; Yang, X. Colorimetric detection of mercury(II) ion using unmodified silver nanoparticles and mercury-specific oligonucleotides. ACS Applied Materials & Interfaces, 2010, 2 (2), pp. 339-342.

5. Giovannozzi, A.M.; Rolle, F.; Sega, M.; Abete, M.C.; Marchis D.; Rossi, A.M. Rapid and sensitive detection of melamine in milk with gold nanoparticles by surface enhanced Raman scattering. Food Chemistry, 2014, 159, pp. 250-256.

6. Suvith, V.S.; Philip, D. Catalytic degradation of methylene blue using biosynthesized gold and silver nanoparticles. Spectrochimica Acta Part A, 2014, 118, pp. 526-532.

7. Saxena, A.; Tripathi, R.M.; Zafar, F.; Singh, P. Green synthesis of silver nanoparticles using aqueous solution of *Ficus benghalensis* leaf extract and characterization of their antibacterial activity. Materials Letters, 2012, 67 (1), pp. 91-94.

8. Liu, P.; Yang, X.; Sun, S.; Wang, Q.; Wang, K.; Huang, J.; Liu, J.; He, L. Enzyme-free colorimetric detection of DNA by using gold nanoparticles and hybridization chain reaction amplification. Analytical Chemistry, 2013, 85 (16), pp. 7689-7695.

9. Stewart, A.; Murray, S.; Bell, S.E.J. Simple preparation of positively charged silver nanoparticles for detection of anions by surface-enhanced Raman spectroscopy. Analyst, 2015, 140 (9), pp. 2988-2994.

10. Tang, Y.; Yang, Q.; Wu, T.; Liu, L.; Ding, Y.; Yu, B. Fluorescence enhancement of cadmium selenide quantum dots assembled on silver nanoparticles and its application to glucose detection. Langmuir, 2014, 30 (22), pp. 6324-6330.

11. Stiles, P.L.; Dieringer, J.A.; Shah, N.C.; Van Duyne, R.P. Surface-enhanced Raman spectroscopy. Annual Review of Analytical Chemistry, 2008, 1 (1), pp. 601-626.

12. Tyler, T.P.; Henry, A.-I.; Van Duyne, R.P.; Hersam, M.C. Improved Monodispersity of Plasmonic Nanoantennas via Centrifugal Processing. Journal of Physical Chemistry Letters, 2011, 2, pp. 218-222.

13. Li, Z.; Xu, H. Nanoantenna effect of surface-enhanced Raman scattering: managing light with plasmons at the nanometer scale. Advances in Physics, 2016, 1 (3), pp. 492-521.

14. Kessentini, S.; Barchiesi, D.; D'Andrea, C.; Toma, A.; Guillot, N.; Di Fabrizio, E.; Fazio, B.; Maragó, O.M.; Gucciardi, G.; de la Chapelle, M.L. Gold Dimer Nanoantenna with Slanted Gap for Tunable LSPR and Improved SERS. The Journal of Physical Chemistry C, 2014, 118, pp. 3209-3219.

15. López-López, M.; García-Ruiz, C. Infrared and Raman spectroscopy techniques applied to identification of explosives. TrAC Trends in Analytical Chemistry, 2014, 54, pp. 36-44.

16. Tuma, R. Raman spectroscopy of proteins: from peptides to large assemblies. Journal of Raman Spectroscopy, 2005, 36 (4), pp. 307-319.

17. Mazzella, W.D.; Buzzini, P. Raman spectroscopy of blue gel pen inks. Forensic Science International, 2005, 152 (2-3), pp. 241-247.

18. Frías, M.; Martínez-Ramírez, S. Use of micro-Raman spectroscopy to study reaction kinetics in blended white cement pastes containing metakaosalem. Journal of Raman Spectroscopy, 2009, 40 (12), pp. 2063-2068.

19. Valley, N.; Greeneltch, N.; Van Duyne, R.P.; Schatz, G.C. A look at the origin and magnitude of the chemical contribution to the enhancement mechanism of surface-enhanced Raman spectroscopy (SERS): theory and experiment. The Journal of Physical Chemistry Letters, 2013, 4 (16), pp. 2599-2604.

20. Esenturk, E.N.; Walker, A.R.H. Surface-enhanced Raman scattering spectroscopy via gold nanostars. Journal of Raman Spectroscopy, 2009, 40 (1), pp. 86-91.

21. Green, M.; Liu, F.M. SERS substrates fabricated by island lithography: the silver/pyridine system. The Journal of Physical Chemistry B, 2003, 107 (47), pp. 13015-12021.

22. He, D.; Yao, Q.-F.; Wang, K.; Yu, S.-H. Large-scale synthesis of flexible free-standing SERS substrates with high sensitivity: electrospun PVA nanofibers embedded with controlled alignment of silver nanoparticles. ACS Nano, 2009, 3 (12), pp. 3993-4002.

23. Sharma, B.; Cardinal, M.F.; Kleinman, S.L.; Greeneltch, N.G.; Frontiera, R.R.; Blaber, M.G.; Schatz, G.C.; Van Duyne, R.P. High-performance SERS substrates: advances and challenges. MRS Bulletin, 2013, 38 (8), pp. 615-624.

24. Salafi, T.; Zeming, K.K.; Zhang, Y. Advancements in microfluidics for nanoparticle separation. Lab on a Chip, 2017,17 (11), pp. 11-33.

25. Ho, C.M.B.; Ng, S.H.; Li, K.H.H.; Yoon, Y.-J. 3D printed microfluidics for biological applications. Lab on a Chip, 2015, 15 (18), pp. 3627-3637.

26. Walter, A.; März, A.; Schumacher, W.; Rösch, P.; Popp, J. Towards a fast, high specific and reliable discrimination of bacteria on strain level by means of SERS in a microfluidic device. Lab on a Chip, 2011, 11 (6), pp. 1013-1021.

27. Li, Q.; Li, B.; Wang, Y. Surface-enhanced Raman scattering microfluidic sensor. RSC Advances, 2013, 3, pp. 13015-13026.

28. Kant, K.; Abalde-Cela, S. Surface-Enhanced Raman Scattering Spectroscopy and Microfluidics: Towards Ultrasensitive Label-Free Sensing. Biosensors, 2018, 62 (8), pp. 1-16.

29. Pu, H.; Xiao, W.; Sun, D.-W. SERS-microfluidic systems: A potential platform for rapid analysis of food contaminants. Trends in Food Science & Technology, 2017, 70, pp. 114-126.

30. Wang, Y.; Rauf, S.; Grewal, Y.S.; Spadafora, L.J.; Shiddiky, M.J.A.; Cangelosi, G.A.; Schlücker, S.; Trau, M. Duplex Microfluidic SERS Detection of Pathogen Antigens with Nanoyeast Single-Chain Variable Fragments. Analytical Chemistry, 2014, 86 (19), pp. 9930-9938.

31. Jahn, I.J.; Zukovskaja, O.; Zheng, X.-S.; Weber, K.; Bocklitz, T.W.; Cialla-May, D.; Popp, J. Surface-enhanced Raman spectroscopy and microfluidic platforms: challenges, solutions and potential applications. Analyst, 2017, 142 (7), pp. 1022-1047.

32. Kim, D.; Campos, A.R.; Datt, A.; Gao, Z.; Rycenga, M.; Burrows, N.D.; Greeneltch, N.G.; Mirkin, C.A.; Murphy, C.J.; Van Duyne, R.P.; Haynes, C.L. Microfluidic-SERS devices for one shot limit-of-detection. Analyst, 2014, 139 (13), pp. 3227-3234.

33. Chen, G.; Wang, Y.; Wang, H.; Cong, M.; Chen, L.; Yang, Y.; Geng, Y.; Li, H.; Xu, S.; Xu, W. A highly sensitive microfluidics system for multiplexed surface-enhanced Raman scattering (SERS) detection based on Ag nanodot arrays. RSC Advances, 2014, 4, pp. 54434-54440.

34. Zhao, H.-Z.; Xu, Y.; Wang, C.-Y.; Wang, R.; Xiang, S.-Y.; Chen, L. Design and fabrication of a microfluidic SERS chip with integrated Ag film@nanoAu. RSC Advances, 2016, 6, pp. 14105-14111.

35. Parisi, J.; Dong, Q.; Lei, Y. *In situ* microfluidic fabrication of SERS nanostructures for highly sensitive fingerprint microfluidic-SERS sensing. RSC Advances, 2015, 5, pp. 14081-14089.

36. Bai, S.; Serien, D.; Hu, A.; Sugioka, K. 3D Microfluidic Surface-Enhanced Raman Spectroscopy (SERS) Chips Fabricated by All-Femtosecond-Laser-Processing for Real-Time Sensing of Toxic Substances. Advanced Functional Materials, 2018, 28, 1706262, pp. 1-10.

37. Gao, R.; Ko, J.; Cha, K.; Jeon, J.H.; Rhie, G.; Choi, J.; deMello, A.J.; Choo, J. Fast and sensitive detection of an anthrax biomarker using SERS-based solenoid microfluidic sensor. Biosensors and Bioelectronics, 2015, 72, pp. 230-236.

38. Lu, X.; Samuelson, D.R.; Xu, Y.; Zhang, H.; Wang, S.; Rasco, B.A.; Xu, J.; Konkel, M.E. Detecting and Tracking Nosocomial Methicillin-Resistant *Staphylococcus aureus* Using a Microfluidic SERS Biosensor. Analytical Chemistry, 2013, 85, pp. 2320-2327.

39. Strehle, K.R.; Cialla, D.; Rösch, P.; Henkel, T.; Köhler, M.; Popp, J. A Reproducible Surface-Enhanced Raman Spectroscopy Approach. Online SERS Measurements in a Segmented Microfluidic System. Analytical Chemistry, 2007, 79 (4), pp. 1542-1547.

40. Lee, P.C.; Meisel, D. Adsorption and surface-enhanced Raman of dyes on silver and gold sols. The Journal of Physical Chemistry, 1982, 86, pp. 3391-3395.

41. Agnihotri, S.; Mukherji, S.; Mukherji, S. Size-controlled silver nanoparticles synthesized over the range 5–100 nm using the same protocol and their antibacterial efficacy. RSC Advances, 2014, 4, pp. 3974-3983.

42. Song, Y.-J.; Wang, M.; Zhang, X.-Y.; Wu, J.-Y.; Zhang, Y. Investigation on the role of the molecular weight of polyvinyl pyrrolidone in the shape control of high-yield silver nanospheres and nanowires. Nanoscale Research Letters, 2014, 9 (17), pp. 1-8.

43. Chen, D.; Qiao, X.; Qiu, X.; Chen, J.; Jiang, R. Convenient, rapid synthesis of silver nanocubes and nanowires via a microwave-assisted polyol method. Nanotechnology, 2010, 21, 025607, pp. 1-7.

44. Yu, D.; Yam, V. Controlled Synthesis of Monodisperse Silver Nanocubes in Water. Journal of the American Chemical Society, 2014, 126, pp. 13200-13201.

45. Zhou, S.; Li, J.; Gilroy, K.D.; Tao, J.; Zhu, C.; Yang, X.; Sun, X.; Xia, Y. Facile Synthesis of Silver Nanocubes with Sharp Corners and Edges in an Aqueous Solution. ACS Nano, 2016, 10 (11), pp. 9861-9870.

46. Métraux, G.S.; Mirkin, C.A. Rapid Thermal Synthesis of Silver Nanoprisms with Chemically Tailorable Thickness. Advanced Materials, 2005, 17 (4), pp. 412-415.

47. Jin, R.; Cao, Y.; Mirkin, C.A.; Kelly, K.L.; Schatz, G.C.; Zheng, J.G. Photoinduced Conversion of Silver Nanospheres to Nanoprisms. Science, 2001, 294, pp. 1901-1903.

48. Zheng, X.; Zhao, X.; Guo, D.; Tang, B.; Xu, S.; Zhao, B.; Xu, W.; Lombardi, J.R. Photochemical Formation of Silver Nanodecahedra: Structural Selection by the Excitation Wavelength. Langmuir, 2009, 25, pp. 3802-3807.

49. Murshid, N.; Keogh, D.; Kitaev, V. Optimized Synthetic Protocols for Preparation of Versatile Plasmonic Platform Based on Silver Nanoparticles with Pentagonal Symmetries. Particle & Particle Systems Characterization, 2013, 31, pp. 178-189.

50. Han, H.J.; Yu, T.; Kim, W.-S.; Im, S.H. Highly reproducible polyol synthesis for silver nanocubes. Journal of Crystal Growth, 2017, 469, pp. 48-53.

51. Zhang, C.-H.; Zhu, J.; Li, J.-J.; Zhao, J.-W. Small and Sharp Triangular Silver Nanoplates Synthesized Utilizing Tiny Triangular Nuclei and Their Excellent SERS Activity for Selective Detection of Thiram Residue in Soil. ACS Applied Materials & Interfaces, 2017, 20 (9), pp. 17387-17398.

52. Grimes, A.; Breslauer, D.N.; Long, M.; Pegan, J.; Lee, L.P.; Khine, M. Shrinky-Dink microfluidics: rapid generation of deep and rounded patterns. Lab on a Chip, 2008, 8 (1), pp. 170-172.

53. Chen, C.-S.; Breslauer, D.N.; Luna, J.I.; Grimes, A.; Chin, W.-C.; Lee, L.P.; Khine, M. Shrinky-Dink microfluidics: 3D polystyrene chips. Lab on a Chip, 2008, 8 (4), pp. 622-624.

54. Sun, M.; Xie, Y.; Zhu, J.; Li, J.; Eijkel, J.C.T. Improving the Resolution of 3D-Printed Molds for Microfluidics by Iterative Casting-Shrinkage Cycles. Analytical Chemistry, 2017, 89 (4), pp. 2227-2231.

55. Ackermann, K.R.; Henkle, T.; Popp, J. Quantitative Online Detection of Low-Concentrated Drugs via a SERS Microfluidic System. ChemPhysChem, 2007, 8, pp. 2665-2670.

56. Yan, W.; Yang, L.; Chen, J.; Wu, Y.; Wang, P.; Li, Z. In Situ Two-Step Photoreduced SERS Materials for On-Chip Single-Molecule Spectroscopy with High Reproducibility. Advanced Materials, 2017, 29, 1702893.

57. Wu, Y.; Jiang, Y.; Zheng, X.; Jia, S.; Zhu, Z.; Ren, B.; Ma, H. Facile fabrication of microfluidic surface-enhanced Raman scattering devices via lift-up lithography. Royal Society Open Science, 2018, 5, 172034.

58. López, I.; Vázquez, A.; Hernández-Padrón, G.H.; Gómez, I. Electrophoretic deposition (EPD) of silver nanoparticles and their application as surface-enhanced Raman scattering (SERS) substrates. Applied Surface Science, 2013, 280, pp. 715-719.

59. Farooq, S.; de Araujo, R.E. Engineering a Localized Surface Plasmon Resonance Platform for Molecular Biosensing. Open Journal of Applied Sciences, 2018, 8, pp. 126-139.

60. Paramelle, D.; Sadovoy, A.; Gorelik, S.; Free, P.; Hobley, J.; Fernig, D.G. A rapid method to estimate the concentration of citrate capped silver nanoparticles from UV-visible light spectra. Analyst, 2014, 139, pp. 4855-4861.

61. Polte, J.; Tuaev, X.; Wuithschick, M.; Fischer, A.; Thuenemann, A.F.; Rademann, K.; Kraehnert, R.; Emmerling, F. Formation Mechanism of Colloidal Silver Nanoparticles: Analogies and Differences to the Growth of Gold Nanoparticles. ACS Nano, 2012, 6(7), pp. 5791-5802.

62. Pillai, Z.S.; Kamat, P.V. What factors control the size and shape of silver nanoparticles in the citrate ion reduction method? Journal of Physical Chemistry B, 2004, 108, pp. 945-951.

63. Frank, A.J.; Cathcart, N.; Maly, K.E.; Kitaev, V. Synthesis of Silver Nanoprisms with Variable Size and Investigation of Their Optical Properties: A First-Year Undergraduate Experiment Exploring Plasmonic Nanoparticles. Journal of Chemical Education, 2010, 87 (10), pp.1098-1101.

64. Abkhalimov, E.V.; Timofeev, A.A.; Ershov, B.G. Electrochemical mechanism of silver nanoprisms transformation in aqueous solutions containing the halide ions. Journal of Nanoparticle Research, 2018, 20 (26), pp. 1-12.

65. Haber, J.; Sokolov, K. Synthesis of Stable Citrate-Capped Silver Nanoprisms. Langmuir 2017, 33 (40), pp. 10525–10530.

66. Zheng, X.; Zhao, X.; Guo, D.; Tang, B.; Xu, S.; Zhao, B.; Xu, W. Photochemical Formation of Silver Nanodecahedra: Structural Selection by the Excitation Wavelength. Langmuir, 2009, 25, pp. 3802-3807.

67. Wang, Q.; Cui, X.; Guan, W.; Zhang, L.; Fan, X.; Shi, Z.; Zheng, W. Shape-dependent catalytic activity of oxygen reduction reaction (ORR) on silver nanodecahedra and nanocubes. Journal of Power Sources, 2014, 269, pp. 152-157.

68. Murshid, N.; Keogh, D.; Kitaev, V. Optimized Synthetic Protocols for Preparation of Versatile Plasmonic Platform Based on Silver Nanoparticles with Pentagonal Symmetries. Particle & Particle Systems Characterization, 2014, 31 (2), pp. 178-189.

69. Anh, M.N.T.; Nguyen, D.T.D.; Thanh, N.V.K.; Phong, N.T.P.; Nguyen, D.H.; Nguyen-Le, M.T. Photochemical Synthesis of Silver Nanodecahedrons under Blue LED Irradiation and Their SERS Activity, Processes, 2020, 8 (3), 292.

70. Xu, P.; Kang, L.; Mack, N.H.; Schanze, K.S.; Han, X.; Wang, H.-L. Mechanistic understanding of surface plasmon assisted catalysis on a single particle: cyclic redox of 4-aminothiophenol, Scientific Reports, 2013, 3, 2997.